Noname manuscript No.
(will be inserted by the editor)

Fully-coupled simulations of megathrust earthquakes and tsunamis in the Japan Trench, Nankai Trough, and Cascadia Subduction Zone

Gabriel C. Lotto · Tamara N. Jeppson · Eric M. Dunham

Abstract Subduction zone earthquakes can produce significant seafloor deformation and devastating tsunamis. Real subduction zones display remarkable diversity in fault geometry and structure, and accordingly exhibit a variety of styles of earthquake rupture and tsunamigenic behavior. We perform fully-coupled earthquake and tsunami simulations for three subduction zones: the Japan Trench, the Nankai Trough, and the Cascadia Subduction Zone. We use data from seismic surveys, drilling expeditions, and laboratory experiments to construct detailed 2D models of the subduction zones with realistic geometry, structure, friction, and prestress. Greater prestress and rate-and-state friction parameters that are more velocity-weakening generally lead to enhanced slip, seafloor deformation, and tsunami amplitude. The Japan Trench's small sedimentary prism enhances shallow slip but has only a small effect on tsunami height. In Nankai where there is a prominent splay fault, frictional parameters and off-fault material properties both influence the choice of rupture pathway in complex ways. The splay generates tsunami waves more efficiently than the décollement. Rupture in Cascadia is buried beneath the seafloor but causes a tsunami that is highly complex due to the rough seafloor bathymetry. Neglecting compliant sediment layers leads to substantially different rupture behavior and tsunami height. We demonstrate that horizontal seafloor displacement is a major contributor to tsunami generation in all subduction zones studied. We document how the non-hydrostatic response of the ocean at short wavelengths smooths the initial tsunami source relative to commonly used approach for setting tsunami initial conditions. Finally, we determine self-consistent tsunami initial conditions by isolating tsunami waves from seismic and acoustic waves at a final simulation time and backpropagating them to their initial state using an adjoint method. We find no evidence to support claims that horizontal momentum transfer from the solid Earth to the ocean is important in tsunami generation.

Keywords tsunami; megathrust earthquake; subduction zone; Japan Trench; Nankai Trough; Cascadia Subduction Zone; tsunami modeling; initial conditions; dynamic rupture

G.C. Lotto · E.M. Dunham
Department of Geophysics, Stanford University, Stanford, CA, USA
E-mail: glotto@stanford.edu

T.N. Jeppson
Department of Geology and Geophysics, Texas A and M University, College Station, TX, USA

E.M. Dunham
Institute for Computational and Mathematical Engineering, Stanford University, Stanford, CA, USA

1 Introduction

Subduction zones span the surface of the Earth and host the world's largest earthquakes and tsunamis. Despite their ubiquity in convergent margins, subduction zones are qualitatively and quantitatively distinct from one another in several ways that greatly influence earthquake rupture and tsunamigenesis. To this point, most models of subduction zone earthquakes have been highly idealized, and none have attempted to couple dynamic rupture to tsunami generation in a realistic setting. In this study, we perform fully-coupled simulations of subduction zone earthquakes and tsunamis in order to gain insight on the following: the influence of geometry, geologic structure, friction, and stress on the megathrust rupture process; the role of horizontal and vertical seafloor motion in contributing to tsunami height; and the extent to which the standard tsunami

modeling procedure makes justifiable assumptions, especially with respect to initial conditions.

We begin by highlighting some of the areas of greatest difference between subduction zones, motivating our interest in modeling specific detail in addition to general subduction features. Decades of seismic imaging has revealed major differences in geometry from one subduction zone to the next (e.g., [13, 42, 57, 61, 62]). Geometrical differences include the presence or absence of splay faults, which have been observed since the 1970s, most notably in Alaska [69], Costa Rica [87], and Nankai [66]. Virtually all subduction zones feature compliant prisms of weakly consolidated sediments, though these vary widely in their landward extent between different subduction zones [102] and along-strike within the same convergent margin (e.g., [62]). Various ocean drilling projects have demonstrated the extreme elastic compliance of sedimentary prisms in Cascadia [97], Nankai [71], Costa Rica [19], Barbados [96], and Tohoku [32, 61], and while exact values of elastic moduli of sediments vary from margin to margin, they are typically one or more orders of magnitude smaller than elastic moduli from deeper parts of the subduction zone. Lab and drilling results are consistent with estimates of rigidity from subduction zone earthquake data, which pin on-fault shear moduli between 1 and 10 GPa at shallow depths [6].

In addition to prism size and material compliance, the thickness of sediments on the incoming crust varies between subduction zones. Sediment thickness, along with crustal age and convergence rate, helps to control the temperature on the fault and thus the updip and downdip limits of velocity-weakening friction and possibly seismicity [64]. The updip limit of seismicity has generally been associated with the dehydration of stable-sliding smectite clays to velocity-weakening illite and chlorite as temperature increases with depth [27, 28, 103]. Field and laboratory data indicate that this transformation occurs at temperatures between 100°C and 150°C (e.g., [25,31,59]). These transitional temperatures occur at depths between 2 and 10 km, depending on the subduction zone [64]. The downdip limit of seismicity may also be determined in part by a velocity-weakening to velocity-strengthening transition, relating to increasing temperatures or mineral transformations [7, 56, 99].

Plate geometry and tectonic forces, which determine the absolute state of stress in a subduction zone, vary around the world. Excess pore pressure is another major determinant of effective stress [74]. As initially saturated seafloor sediments subduct and pressurize, they expel water through porosity reduction and mineral dehydration. Here, too, we observe differences between subduction zones, where fluid pressures in sedimentary prisms are often elevated but can fall anywhere in the range between hydrostatic and lithostatic [59]. Fluid expulsion rate can vary depending on whether a margin is accretionary or nonaccretionary, and on the overall permeability of a fault zone [74].

Given such a diversity in qualitative and quantitative subduction zone characteristics, it should not surprise us to find substantial differences in rupture style and tsunamigenic efficiency. Tsunamis from great megathrust events like the M_w 9.1-9.3 2004 Sumatra earthquake [91] result in significant loss of life and cause massive damage to property and infrastructure, but so do those from more-efficient tsunami earthquakes that release hundreds of times less energy, such as the M_w 7.7 2010 Mentawai event [46]. Meanwhile, other major significant subduction zone earthquakes like the M_w 8.6 2005 Nias-Simeulue event [8] generate only small tsunamis that do limited damage. The non-monotonicity of the relationship between earthquake magnitudes and tsunami heights should cause us to ask which specific properties of subduction zones influence tsunami generation, and to what extent they do so.

The first major focus of this study is how geometry, friction, stress, and material structure influence rupture and the ensuing tsunami. We can link several subduction zone characteristics to differences in earthquake rupture and tsunamigenic behavior. For instance, fault and seafloor geometry is a prominent factor in determining tsunami amplitude. A steeply-dipping décollement or splay fault will produce a larger portion of vertical uplift, which directly corresponds to tsunami height (e.g., [12, 34]). The angle of a sloping seafloor, including the presence of seamounts or any rough bathymetry, also directly contributes to tsunami height even if seafloor motion is entirely horizontal [48, 93]. Several studies [12, 34, 111] have used dynamic rupture simulations of branching faults to demonstrate that prestress, frictional properties, and rupture velocity are important in determining rupture pathway, e.g. whether an earthquake ruptures along a steep splay, a flatter décollement, or both. The results of our Nankai simulations, presented below, bear out the importance of prestress and friction on the choice of rupture pathway.

In addition to determining rupture pathway, fault friction and prestress (particularly the contributions of excess pore pressure) help to control both rupture speeds and long-term deformation [51,74,104]. Our previous work shows that the choice of rate-and-state frictional parameter $b - a$ has a major influence on rupture velocity, total

slip, and tsunami height for a simple subduction-zone-like geometry [50]. That same work demonstrates the effect of compliant prism materials on earthquake rupture and tsunami amplitude. In Lotto et al. [50] we find that larger, more compliant prisms in a purely elastic medium lead to enhanced shallow slip and greater tsunami amplitudes. One can invoke Hooke's Law to simply account for this effect: A more compliant material will be more susceptible to elastic deformation for a given earthquake-induced stress change. (Alternatively, Ma [51] argues that sedimentary prisms are subject to significant inelastic deformation during shallow subduction zone earthquakes.) Additionally, normal stress perturbations caused by slip on a bimaterial interface—commonly found in shallow subduction zone faults—can alter earthquake rupture and lead to unstable slip [3, 52, 110]. Aldam et al. [1] find that several physical quantities, including slip velocity and normal stress drop, exhibit a nonmonotonic dependence on the bimaterial contrast.

Simulations and empirical results from real earthquakes support the idea that compliant prisms have a large effect on earthquake rupture. Numerical experiments by Tamura and Ide [92] of a branching fault system in a heterogeneous medium with a free surface show that when the upper medium is more compliant, rupture is encouraged on the branching fault. Several slow-rupturing tsunami earthquakes have been associated with shallow slip through subducted sediments [36, 70, 78, 94]. Gulick et al. [22] argue that dewatering and lithification of shallow sediments in the Sumatra-Andaman margin made them strong enough to enable shallow rupture during the 2004 Sumatra earthquake.

No single conceptual model fully captures the variations between subduction zones [102]. And while many numerical studies of dynamic rupture focus on the effects of varying one parameter, recent publications have shown that dynamic rupture experiments produce nonmonotonic or counterintuitive results, especially when multiple variables are introduced [1, 50]. Given the extensive qualitative and quantitative differences between subduction zones and the extent to which those differences affect rupture and tsunamigenesis, it is necessary to model individual subduction zones in some sufficient level of detail in order to make reasonable conclusions about tsunami hazard. In this study we consider earthquake rupture and tsunami generation for three distinct subduction zones: the Japan Trench, the Nankai Trough, and the Cascadia subduction zone. We model each subduction zone in 2D with realistic geometry and material properties, and make reasonable choices for friction, prestress, and pore pressure.

In addition to exploring the effects of using realistic frictional and structural parameters, we are also motivated by some more fundamental questions about the physics of tsunami generation. To what extent does horizontal deformation of the seafloor contribute to sea surface uplift? Do common tsunami modeling techniques make valid assumptions about tsunami generation and propagation?

We are presently aware of only three modeling approaches—ours [49] and two others [53,76]—that attempt the fully coupled problem of dynamic rupture and tsunami generation. Typical tsunami generation approaches separate the problem into several distinct steps: determination of fault slip, calculation of seafloor deformation, and translation of that deformation into the ocean to provide tsunami initial conditions. Breaking the problem up this way requires making several approximations, not all of which may be justified.

Tanioka and Satake [93] first theorized the role that horizontal motion of a sloping seafloor plays in determining the initial height of a tsunami. The Tanioka and Satake initial tsunami height, η_{ts}, superimposes the obvious effect of vertical seafloor displacement, u_y, with the kinematic effect of horizontal displacement, u_x, of a seafloor with slope m, and translates that motion to the sea surface under the assumption of hydrostatic ocean response:

$$\eta_{ts}(x) = u_y(x) - m(x)u_x(x). \tag{1}$$

Though the contribution of horizontal displacement to ocean uplift (Figure 1) was recognized over two decades ago, most tsunami models continue to neglect the second term in equation (1). Likewise, most tsunami models also do not account for Kajiura's [33] nonhydrostatic correction to the initial tsunami height, which acts as a low-pass filter, reducing the contribution of short-wavelength seafloor deformation to ocean uplift. Additionally, tsunami propagation models based on the shallow water wave equation neglect dispersion, which is another consequence of nonhydrostatic ocean response at wavelengths comparable to or less than the ocean depth. Numerical methods that decouple the earthquake rupture and tsunami generation process also inherently ignore the compressibility of the ocean. Many also neglect the time-dependent nature of the rupture process.

In addition to the kinematic effects of horizontal seafloor motion described above, Song and others (e.g., [89, 90]) have argued that horizontal momentum transfer from the solid Earth to the ocean is a major contributor to tsunami height. We have previously found that such an effect is negligible for subduction zone earthquakes [48], at least

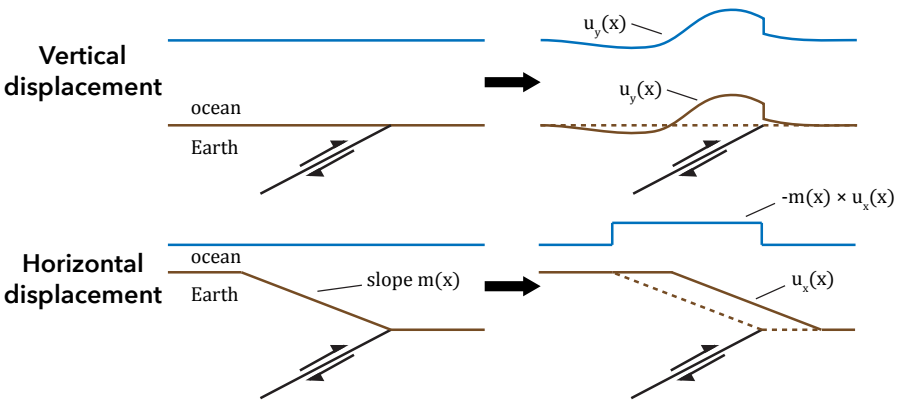

Fig. 1 The role of vertical and horizontal seafloor deformation in setting initial sea surface height, according to the theory of Tanioka and Satake [93] and equation (1). Figure redrawn from that publication.

for the specific geometries studied in that work. Fully-coupled methods like ours naturally account for momentum transfer, whereas typical tsunami models neglect it by setting initial horizontal velocity in the ocean to zero.

To what extent are these sundry assumptions valid for real subduction zone earthquakes? Through our simulations we aim to determine the relevance of the following factors on tsunami generation and propagation: horizontal seafloor displacement, non-hydrostatic corrections to η_{ts}, tsunami dispersion, ocean compressibility, and a time-dependent rupture process.

2 Modeling Framework

We perform fully-coupled simulations of earthquakes and tsunamis at three subduction zones using 2D profiles centered at the oceanic trench and extending hundreds of kilometers both landward and seaward. Seafloor and fault geometries as well as material properties are based upon seismic surveys and ocean drilling experiments. Our models reflect the complexities of seafloor bathymetry and include major fault bends, although we do not explicitly consider short wavelength fault roughness or a finite-width fault damage zone. The subduction zone models also capture complexities in geology where they are known to exist, including smoothly varying material properties, compliant prisms, subducted sediments, and mantle wedges.

We simulate coupled earthquakes and tsunamis using a provably stable and high-order accurate finite difference code that couples an acoustic ocean in the presence of gravity to an elastodynamic Earth [45]. Surface gravity waves are incorporated via a linearized boundary condition that imposes gravity on perturbations about an ocean initially in hydrostatic balance [49]. This approach allows us to model the full seismic, ocean acoustic and tsunami wavefield in one self-consistent framework. Tsunami waves are generated by time-dependent seafloor deformation in response to dynamic earthquake rupture, and propagate dispersively in a compressible ocean.

Dynamic rupture is modeled on the plate boundary fault—and on a splay fault, for Nankai–using a differential form of rate-and-state friction described by Kozdon and Dunham [43] that alleviates issues of instability and ill-posedness associated with bimaterial interfaces:

$$\frac{\mathrm{d}\tau}{\mathrm{d}t} = \frac{a\bar{\sigma}}{V}\tanh\left(\frac{\tau}{a\bar{\sigma}}\frac{\mathrm{d}V}{\mathrm{d}t}\right) - \frac{|V|}{L}\left[\tau - \bar{\sigma} f_{ss}(V)\right], \quad (2)$$

for time t, shear strength τ, slip velocity V, and state evolution distance L. Effective normal stress $\bar{\sigma}$ is defined as the difference between total normal stress and pore pressure,

$$\bar{\sigma} = \sigma - p. \quad (3)$$

The steady-state friction coefficient, f_{ss}, is dependent on V as

$$f_{ss}(V) = f_0 - (b-a)\ln(V/V_0), \quad (4)$$

where V_0 is a reference velocity and $b-a$ is a dimensionless variable that determines the extent to which friction increases or decreases with increasing slip velocity ($b-a>0$ is velocity-weakening and $b-a<0$ is velocity-strengthening). The parameter f_0 is the friction coefficient for steady sliding at V_0. For all simulations of all subduction zones, we set a constant $V_0 = 10^{-6}$ m/s and $L = 0.8$ m.

We account for undrained poroelastic changes in pore pressure, Δp, in response to changes in total normal stress, $\Delta\sigma$, with a linear relation of the form $\Delta p = B\Delta\sigma$. Considering the poroelastic effect lets us rewrite effective normal stress as [45]

$$\bar{\sigma} = \bar{\sigma}_0 + (1-B)\Delta\sigma, \quad (5)$$

which acts to partially buffer changes to effective normal stress. Equation 5 is a limiting case of a model [10] for a fault that is bounded by damaged material, where B is Skempton's coefficient. Across all simulations, we choose a moderate value of $B = 0.6$ (where in the $B \to 1$ limit, effective stress would remain constant).

At the coast of each of our subduction zone models is a vertical "cliff," a nonphysical feature that allows us to include a clear ocean-Earth boundary and has no effect on earthquake rupture or the first few hundred seconds of tsunami propagation in the open ocean. The cliff tends to produce its own tsunami signal as it moves horizontally in response to seismic waves, but this tsunami is not a realistic feature.

For each subduction zone simulation, grid points along the fault are separated by about 200 m, though this varies because of the curved geometry. The time step size is 5×10^{-4} s. This allows us to accurately capture wave frequencies lower than ~ 0.5 Hz, though the frequency resolution is reduced in low velocity layers. At distances hundreds of kilometers away from the fault, we progressively stretch the grid to place the outer boundaries far from the region of interest so that numerical reflections are unnoticeable.

In the following sections, we introduce our three subduction zones of interest, justify our choices of physical parameters, and present results for each subduction zone. This is followed by a comprehensive discussion of the more general issues raised in this introduction.

3 Japan Trench - Background

The 2011 M_w 9.0 Tohoku earthquake, Japan's most recent great megathrust event, ruptured a large portion of the Japan Trench and generated a devastating tsunami, several meters high in the open ocean [16,65]. Observational and modeling evidence supports the idea that the earthquake ruptured to the trench, rapidly deforming the seafloor by ~20 to 50 m and contributing to the extreme tsunami amplitude [17, 40, 43, 81].

Our model of the Japan Trench uses seafloor and fault geometry that is essentially identical to that of our previous efforts to model the Tohoku event [43,44,48], based on seismic lines from Miura et al. [57], but with somewhat smoother interfaces and bathymetry. The material properties are derived from the structural models of Miura et al. [57] and Nakamura et al. [61]. The structure (Figure 2) features a fairly small accretionary prism that extends 22 km downdip along the décollement, and a 2 km layer of sediments along the seafloor landward of the oceanic trench. The depth of the ocean at the trench is 7.5 km. At the coastline ($x = -220$ km, where $x = 0$ is the trench), the water meets the land in a nonphysical "cliff," as mentioned in section 2. We nucleate the earthquake at a depth of 20.8 km, by quickly increasing shear stress over a small region along the fault.

Dynamic rupture simulations on faults in elastic media require setting several parameters relating to friction and prestress. In order to select a, b, and f_0, we appeal to several experimental results obtained from the Japan Trench Fast Drilling Project (JFAST), conducted during Integrated Ocean Drilling Program Expeditions 343/343T [60]. The JFAST project penetrated a part of the plate boundary fault that had experienced large shallow slip during the 2011 Tohoku earthquake and recovered a core of clay-rich material from 822 m below the seafloor [9]. Additionally, a temperature observatory was installed in the drilled hole through the plate boundary, which recorded temperature observations over a 9-month period [18]. The observed temperature anomaly in the vicinity of the fault corresponded to an apparent friction coefficient of 0.08. High-velocity (1.3 m/s) friction experiments on JFAST fault samples showed very low shear stress and a correspondingly small stress drop [101]. More recent laboratory experiments on Japan Trench material at sub-seismic velocities have found a range of somewhat higher values for the friction coefficient, from 0.17 [23] to 0.20 [29] to ~ 0.35 [82]. Inspired by these data, we run two sets of simulations of the Japan Trench, one using $f_0 = 0.15$ and the other using $f_0 = 0.35$ at shallow depths. At $x < -22$ km the décollement is no longer bounded by a highly compliant sedimentary prism and we transition f_0 from the lower values above to a more moderate value of 0.5 over several kilometers.

There are also several experimental results that measured the rate-and-state parameters a and b for various Japan Trench samples. It is often assumed that clay minerals, which comprise the shallow parts of subduction zone faults, exhibit velocity-strengthening behavior. However, laboratory experiments have shown that the frictional behavior of smectite-rich sediments is not always stable; for example, Saffer and Marrone [73] observed velocity-weakening behavior in smectite at room temperature under low slip velocities. Tests of smectite-rich materials recovered from the Japan Trench showed frictional behavior that is mostly velocity-strengthening but sometimes velocity-weakening or velocity-neutral [29]. More recently, Sawai et al. [82] showed that JFAST core samples exhibited

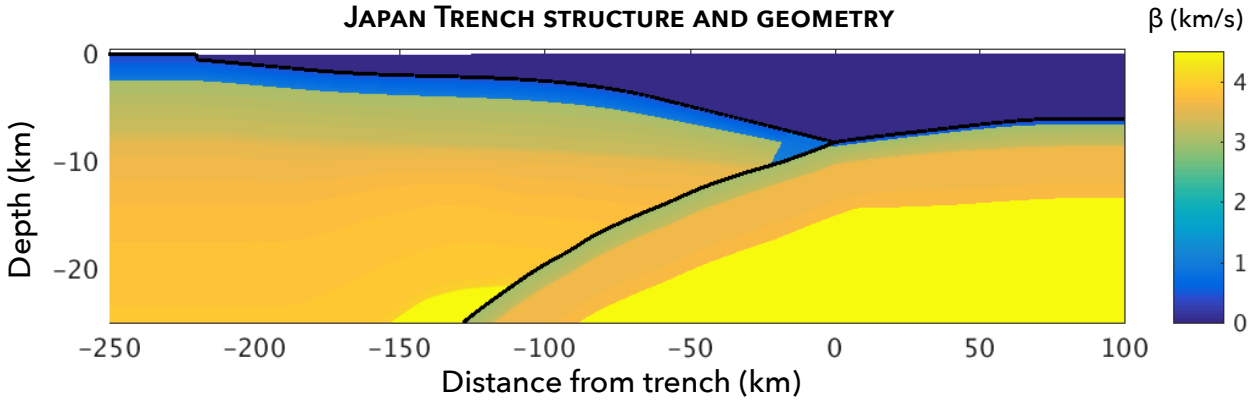

Fig. 2 Material structure and geometry of the Japan Trench used for our simulations, colored by shear wave speed β. Bold black lines trace the plate boundary fault and the seafloor.

both velocity-weakening and velocity-strengthening behavior under a range of combinations of temperature and slip velocity, and that $b-a$ often responded non-monotonically to those variables. Given the poorly constrained nature of shallow friction in subduction zones including the Japan Trench, we run simulations with four different values of $b-a$ in the region adjacent to the prism: $b-a=-0.004, -0.002, 0.000,$ or 0.002.

Deeper in the subduction zone, we set $b-a=0.004$, a solidly velocity-weakening value that allows for earthquake nucleation and propagation at depth. Velocity-weakening friction is required to nucleate an earthquake but this choice of $b-a$ is also supported by results from Sawai et al. [83], who report that blueschist fault rocks, likely present at seismogenic depths at the Japan Trench, exhibit velocity-weakening behavior at temperatures relevant to hypocentral depths. Similarly to f_0, $b-a$ transitions from one of the values above to $b-a=0.004$ as the fault descends past the prism. Downward along the décollement ($x=-180$ km), in order to smoothly cease rupture propagation, we transition the fault from velocity-weakening to strongly velocity-strengthening by gradually increasing the value of a by an order of magnitude.

Since our simulations consider only linear elastic deformation of the solid, stress and pore pressure need only be initialized on the fault. Total normal stress is assumed to increase lithostatically as a function of fault depth below seafloor d as $\sigma=\rho g d$, with $g=9.8$ m/s^2 and density at a constant, nominal value of $\rho=2000$ kg/m^3. This formulation approximates a state of stress in which the minimum principal stress is vertical and the décollement is nearly horizontal.

As equation (3) indicates, pore fluid pressure plays a major role in determining stress on the fault. We introduce the Hubbert-Rubey fluid pressure ratio [26], λ, to quantify pore pressure relative to lithostatic pressure for a submarine fault:

$$\lambda=\frac{p}{\rho g d}. \tag{6}$$

A pore pressure ratio of $\lambda=1$ corresponds to pore pressure that increases lithostatically. For our nominal density of $\rho=2000$ kg/m^3 in the earth, $\lambda=0.5$ means pore pressure increases hydrostatically. Anywhere in between, pore fluid are overpressured. Both Seno [85] and Kimura et al. [39] argue that pore fluid pressure is highly elevated in the Japan Trench, with $\lambda>0.9$ everywhere along the décollement. We ran sets of simulations with $\lambda=0.7$ and $\lambda=0.9$, though we prefer the latter value.

To inhibit excess slip at depth, we follow the example of Rice [72] and assume that below some depth, pore pressure begins to increase lithostatically, i.e. $\lambda=1$, and effective normal stress no longer grows. This occurs at a depth such that the maximum effective normal stress is $\bar{\sigma}_{max}=40$ MPa. We also assume that the fault has some minimum strength near the trench, such that $\bar{\sigma}_{min}=1$ MPa. Initial shear stress along the entire fault is calculated as $\tau=f_0\bar{\sigma}$.

4 Japan Trench - Results

The Japan Trench serves as something of a base case scenario within this study, given its relatively simple geometry and structure and our prior modeling of the 2011 Tohoku earthquake and tsunami [43, 44, 48]. In this section, we present a range of numerical experiments that explore the variability produced by adjusting friction and initial stress.

We first examine the effects of varying the rate-and-state friction parameter $b-a$ in the shallow part of the subduction zone, as in the upper left plot of Figure 3. For the Japan Trench, shallow $b-a$ has a clear but limited effect on slip and

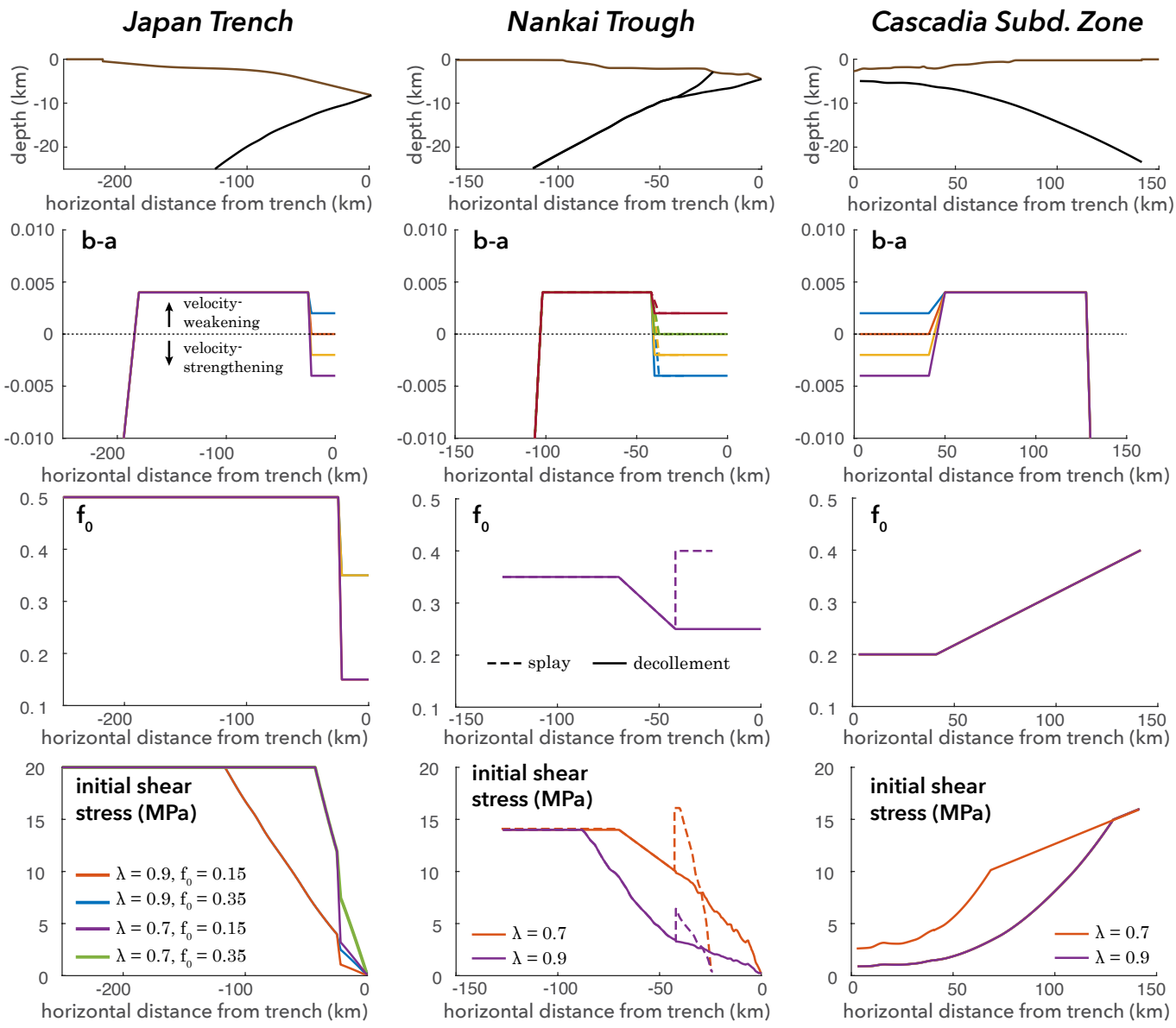

Fig. 3 Initial conditions on frictional parameters $b-a$ and f_0, and shear stress τ, for the three subduction zones considered in this study. For our Japan Trench simulations, we run two sets of simulations, one with $f_0 = 0.15$ and one with $f_0 = 0.35$ near the trench. For each subduction zone, we vary $b-a$ among four options: $b-a = -0.004, -0.002, 0.000,$ and 0.002. We also vary the pore pressure ratio, λ, between 0.7 and 0.9. This leads to two different versions of initial shear stress for Nankai and Cascadia (and four for the Japan Trench, given the two parameterizations of f_0 for that subduction zone). Dashed lines for the Nankai Trough refer to conditions on the splay rather than the plate boundary fault.

on final tsunami height (at $t = 500$ s). Figure 4 shows results for two extreme conditions of stress, $\lambda = 0.9, f_0 = 0.15$ and $\lambda = 0.7, f_0 = 0.35$. In both cases, smaller values of $b-a$ (more velocity-strengthening friction) lead to less slip across the whole fault but especially at the prism, as unstable slip is inhibited near the trench. The effect of changing $b-a$ is greater, as is total slip, for the case with greater initial stress (i.e., $\lambda = 0.7, f_0 = 0.35$). Tsunami height varies in accordance with slip, although in a less noticeable way.

These results fit reasonably well in the context of our previous work on compliant prisms [50], for which we varied compliance, prism size, and shallow $b-a$ in an idealized subduction zone geometry. In that work, we used a structural model where material properties were piecewise constant, having one set of values outside the prism and another set inside the compliant prism. We characterized the compliance of the prism by a nondimensional parameter r, defined as the ratio of shear wave speeds β in the prism and elsewhere in the Earth, $r = \beta_{prism}/\beta_{earth}$. Prism size W was characterized

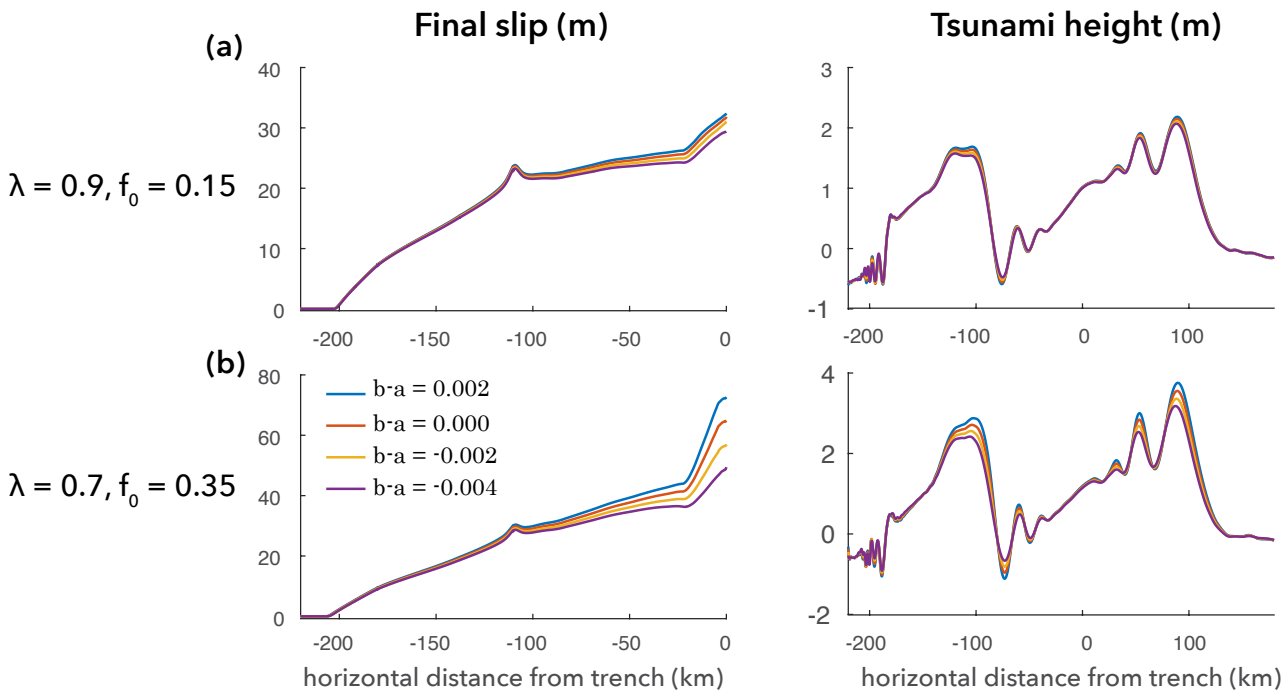

Fig. 4 The effect of modifying rate-and-state parameter $b-a$ on total slip and final tsunami height (time $t = 500$ s) for the Japan Trench, with (a) $\lambda = 0.9, f_0 = 0.15$ and (b) $\lambda = 0.7, f_0 = 0.35$. Increasing $b-a$ makes the shallow part of the fault more susceptible to unstable slip, increasing slip and tsunami height everywhere. This effect is more pronounced for (b), where prestress is higher.

as the downdip extent of the prism. Though the Japan Trench geometry in this study has a more complex structure and initial stress distribution, we can make rough estimates of $W = 22$ km and $r \approx 4$. For those sets of parameters, our previous work shows that $b-a$ has a similarly modest effect on slip and tsunami height (see Fig. 5c and d of Lotto et al. [50]).

We now focus on the effects of the friction coefficient and pore pressure ratio, selecting a moderate value of $b - a = -0.002$ (slightly velocity-strengthening behavior) near the trench and modifying shallow f_0 and λ. In this set of simulations, presented in Figure 5, initial stress (as modified via pore pressure ratio) is the single greatest factor affecting slip, horizontal and vertical seafloor displacement, and tsunami height. Lower initial shear stresses (see lower left plot of Figure 3) lead to lower stress drops (see Supplementary Figure 21) and thus less slip throughout the fault. The effect of f_0 on slip is apparent only beneath the prism where higher f_0 means higher initial shear stress. Changes to f_0 and λ have similar effects on horizontal and vertical seafloor displacement. Differences in tsunami heights are also largely determined by pore pressure ratio, and despite the enhanced slip near the trench with $f_0 = 0.35$, the tsunami—especially its landward wave—barely registers that difference. (Note that the tsunami signal at the far left of Figures 4 and 5e at $x < -175$ km is a wave propagating from the coast toward the ocean, caused by horizontal displacement of the artificial ocean-earth "cliff" during seismic deformation. This byproduct of our structural model is not a realistic feature and would not be observed.)

We now introduce another way to quantify earthquake rupture, seismic potency per distance along strike:

$$P(t) = \int_{l_1}^{l_2} s(l,t)\,\mathrm{d}l, \tag{7}$$

where s is slip and the variable l follows the downdip fault axis from l_1 to l_2. Potency is defined as earthquake moment per unit rigidity; we use potency rather than moment to avoid ambiguities in the choice of rigidity on a bimaterial fault plane. We further define potency rate per distance along strike, $\dot{P}$, as the rate of change in potency over time,

$$\dot{P}(t) = \frac{\mathrm{d}P}{\mathrm{d}t}. \tag{8}$$

We use potency rate to compare and contrast the time-dependent earthquake source process between different simulations. For example, in Figure 5b we see that earthquakes with $\lambda = 0.7$ rupture for

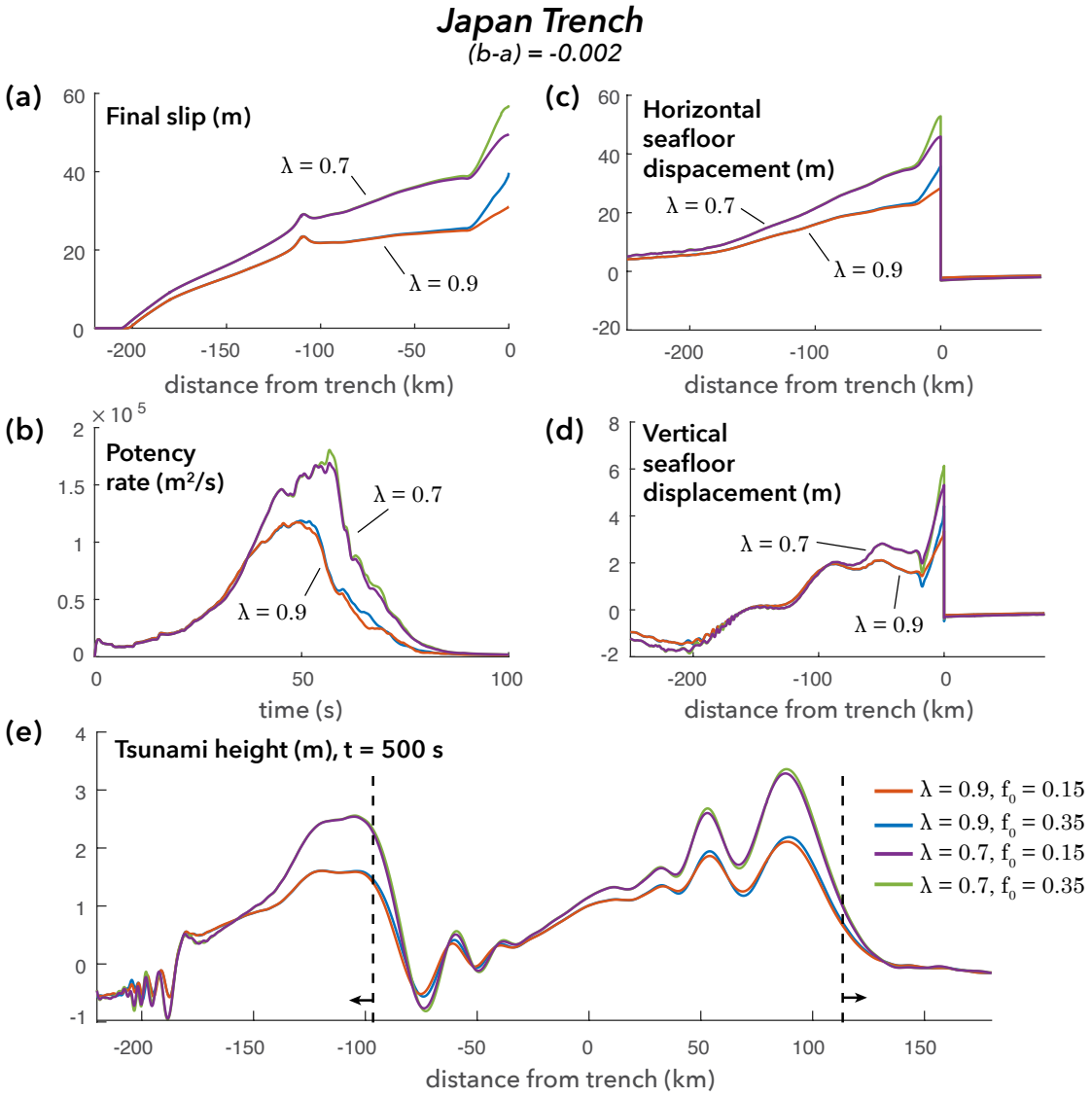

Fig. 5 Modeling results from the Japan Trench, varying f_0 and λ but keeping a constant shallow $b - a = -0.002$ across simulations. Pore pressure ratio, which controls stress drop and hence overall slip, has the greatest influence on (a) slip, (b) potency rate, (c) horizontal seafloor displacement, (d) vertical seafloor displacement, and (e) tsunami height at $t = 500$ s, while shallow f_0 is of secondary importance. Vertical dashed lines mark the distance the fastest tsunami waves produced at $x = 0$ would travel by the final time.

longer and have more total potency than earthquakes with $\lambda = 0.9$, but that going from $f_0 = 0.15$ to $f_0 = 0.35$ only affects the rupture process marginally.

5 Nankai Trough - Background

The Nankai Trough in southern Japan has hosted five M_w 8+ earthquakes since the beginning of the eighteenth century [2]. Each event launched a significant tsunami and caused over 1000 fatalities. The last pair of tsunamigenic earthquakes were the 1944 Tonankai (M_w 8.1) and 1946 Nankaido (M_w 8.3) events. Consequently, the Nankai Trough has been closely studied by earth scientists for decades.

Southeast of Shikoku Island and the Kii Peninsula, the Philippine Sea Plate subducts beneath the Eurasian Plate and produces a very large accretionary prism [66]. The prism, which has been developing since the Miocene, consists of compliant materials, mainly offscraped and underplated from turbidites and Skikoku Basin sediments [67]. The Nankai Trough is distinguished from other subduction zones by its prominent splay fault, a thrust fault that bends up from the megathrust to the seafloor at a higher angle than the décollement [66].

A geodetic slip inversion of the 1944 and 1946 earthquakes by Sagiya and Thatcher [75] suggested a highly complex source process for the two events,

which they associated in part with coseismic slip on splay faults. The presence of splay faults has major implications for tsunami generation; an earthquake rupture that branches off of the main megathrust and continues along a steeper splay could possibly generate a tsunami with a higher amplitude and certainly with a different wave profile than one that continues along the décollement. Though Tanioka and Satake [95], drawing from an inversion of tsunami waveforms from the 1946 event, found that large slip on splay faults was not required to fit available data, other publications have reached the opposite conclusion. Cummins and Kaneda [11] argued that the tsunami data could be matched equally well if all slip was confined to a splay rather than the plate boundary fault.

Scientific opinion is more unified with respect to the 1944 Tonankai event. A topographical argument was made by Kikuchi et al. [38], who reasoned that the repetition of fault motions must be responsible for the rough profile of the Kumano Basin above the inferred slip distribution of the 1944 earthquake. Moore et al. [58], analyzing the results of 2D and 3D seismic reflection surveys, showed that there has been more activity on the splay than on the décollement and concluded that the splay fault likely contributed to the 1944 tsunami. Geothermometric measurements on core samples from the Nankai Trough revealed evidence of frictional heating on shallow portions of both the splay fault and the plate boundary fault, implying that coseismic rupture has occurred on both segments [77].

Several studies, inspired by the splay fault at Nankai, have used numerical models to explore various parameters that influence rupture in the vicinity of a branching fault system. Kame et al. [34] focused on the effects of prestress, rupture velocity, and branch angle (in an unbounded, homogeneous, elastic medium) and found that the prestress has a significant effect on the favored rupture direction, though enhanced dynamic stressing sometimes resulted in slip on a less-favorably oriented segment. Collapsing the geometry of the Nankai Trough into the context of their parameter space study, they predicted that coseismic rupture would follow the splay fault and cause negligible slip along the plate boundary fault. DeDontney and Hubbard [12] expanded on that work, using realistic initial stress states derived from elastic wedge theory and a range of values for friction and dip angle to produce a variety of simulations where rupture propagated along the main fault, a branching fault, or both. Simulating dynamic rupture in 3D, Wendt et al. [111] observed rupture remaining on the plate boundary thrust for a homogeneous prestress, but found that the introduction of a stress barrier leads to activation of splay faults. Tamura and Ide [92], modeling a branching fault system in a 2D bimaterial medium with a free surface, reported that for homogeneous prestress, rupture is enhanced on the branching fault when the upper material is more compliant, as would be likely the case in a subduction zone. These studies advance the hypothesis that rupture on the splay is plausible or even likely, but they greatly simplify the Nankai Trough; our simulations capture realistic geometric and geologic features, with spatially variable prestress and frictional properties.

Our geometric and structural model for Nankai is based upon two seismic profiles extending from the Kii Peninsula out past the trench axis: a wide-angle seismic survey (profile KR9806) interpreted by Nakanishi et al. [62] and waveform tomography images from Kamei et al. [35]. Thus, our model (Figure 6) is representative of the segment of the Nankai Trough through which the 1944 Tonankai earthquake ruptured. A compliant layer of sediments, 1-3 km in thickness, underlies the seafloor and fills the prism bounded by the décollement and splay. At the trench ($x = 0$), the ocean reaches its maximum depth of 5.1 km. The splay branches off the décollement at $x = -42$ km (a depth of 8.5 km) and breaches the seafloor at $x = -24$ km.

Our approach to assigning initial stresses on the fault is somewhat different for Nankai and Cascadia than for Tohoku. Rather than assuming a simple depth dependent normal stress on the faults, we instead opt for the more self-consistent approach of prescribing a stress field everywhere in the solid and resolving it onto the faults. We draw on the work of DeDontney and Hubbard [12], who use critical and elastic wedge theory to determine the stress state of a Nankai-like subduction zone geometry. They characterize the stress state in the prism by a ratio of principal stresses, σ_1/σ_3, and by the angle of σ_1 (the more horizontal principal stress component) relative to the dip of the plate boundary fault, Ψ (Figure 7). For the Nankai-like subduction zone geometry, they determine that $\Psi = 13.5°$ and $\sigma_1/\sigma_3 = 2.28$ are appropriate values. Our approach is to have σ_1 increase lithostatically with depth below seafloor and to scale σ_3 according to the ratio of principal stresses above. The resulting stress state is resolved onto the faults, and the ratio τ/σ on the fault is used to determine an approximate f_0. This approach yields values of $f_0 = 0.4$ on the splay, $f_0 = 0.25$ on the shallow plate boundary thrust, and $f_0 = 0.35$ on the deep plate boundary fault. These values are consistent with experimental results that pin friction on the splay fault between $f_0 = 0.36$ and $f_0 = 0.46$ [23, 30]. The-

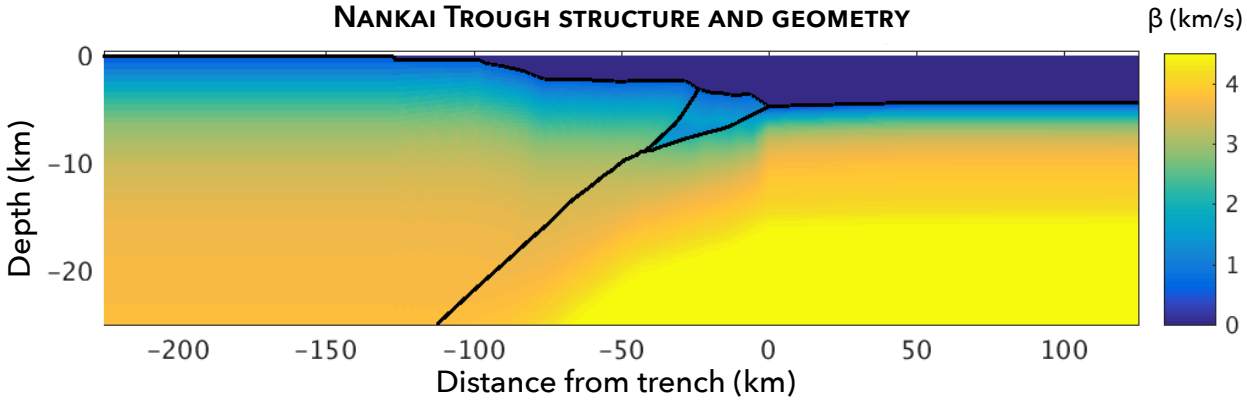

Fig. 6 Material structure and geometry of the Nankai Trough used for our simulations, colored by shear wave speed β. Bold black lines trace the plate boundary fault, the splay fault, and the seafloor.

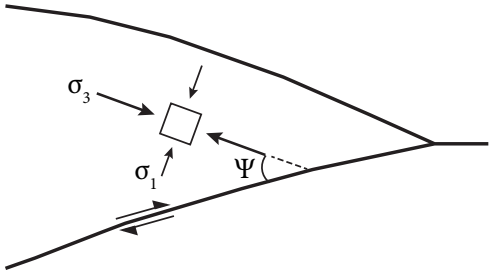

Fig. 7 Principal stresses σ_1 and σ_3 oriented relative to the plate boundary fault by angle Ψ. This stress convention is used to determine the prestress for Nankai and Cascadia.

ory and experimental data for the plate boundary thrust are also supportive but less precise—one estimate has $0.16 \leq f_0 \leq 0.26$ [41] and another finds $0.32 \leq f_0 \leq 0.40$ [30]. For a chosen value of λ, we use equations (6) and (3) to calculate effective normal stress and $\tau = f_0\bar{\sigma}$ to calculate initial shear stress.

With regard to the choice of λ for Nankai simulations, published estimates for pore pressure vary widely between and within studies. While Seno [85] gives a pore pressure ratio as high as $\lambda \approx 0.98$ on the megathrust, other results yield more moderate values of $\lambda \approx 0.8$ and $0.68 \leq \lambda \leq 0.77$ [88, 98]. Pore pressure on the splay is probably similarly elevated, with Tsuji et al. [100] estimating that the pore pressure ratio lies roughly between $\lambda \approx 0.6$ and $\lambda \approx 0.9$. Given the wide spread of estimates of λ and the influence of prestress on the results of dynamic rupture experiments, we run two sets of simulations, one with $\lambda = 0.7$ on both splay and megathrust and another with $\lambda = 0.9$.

To choose rate-and-state parameters a and b, we appeal in part to Ikari and Saffer [30], whose experiments on Nankai Trough sediments showed mostly velocity-strengthening friction, but with significant variability on both the splay and the megathrust. As with the Japan Trench, we run simulations with four possible values of $b-a$ (-0.004, -0.002, 0.000, and 0.002), allowing that parameter to vary independently on the splay and the megathrust for a total of 16 permutations.

6 Nankai Trough - Results

The Nankai Trough is unique in this study, in that rupture nucleated at depth comes to a fault juncture, and can choose between propagating along the steeper splay, the flatter décollement, or both. Because the splay dips at a higher angle and breaks the seafloor surface closer to the coast, the rupture pathway is expected to have serious implications for tsunami hazard. Indeed, we find that the choice of rupture pathway has a qualitative effect on the the tsunami waveform and a quantitative effect on its amplitude.

We start by looking at simulation results where pore pressure ratio is constant at $\lambda = 0.9$ and shallow $b - a$ varies between $b - a = -0.004$ and $b - a = 0.002$. We focus on simulations where $b - a$ is the same on both the splay and décollement; we ran several versions where $b-a$ was different on the two fault segments above the juncture, but there is no particular reason to believe that one segment is more or less velocity-weakening than the other, and we observe plenty of variability in outcomes even when $b - a$ is identical.

Figure 8a shows cumulative slip on the fault for both the splay (dashed lines) and the décollement (solid lines). We see that small changes in $b - a$ result in major changes to the choice of rupture pathway. The most velocity-strengthening model, with $b - a = -0.004$ (blue lines), ruptures very little along the décollement, producing almost zero slip at the trench. However, that same model produces greater slip on the splay than any other model, despite experiencing a relatively low stress

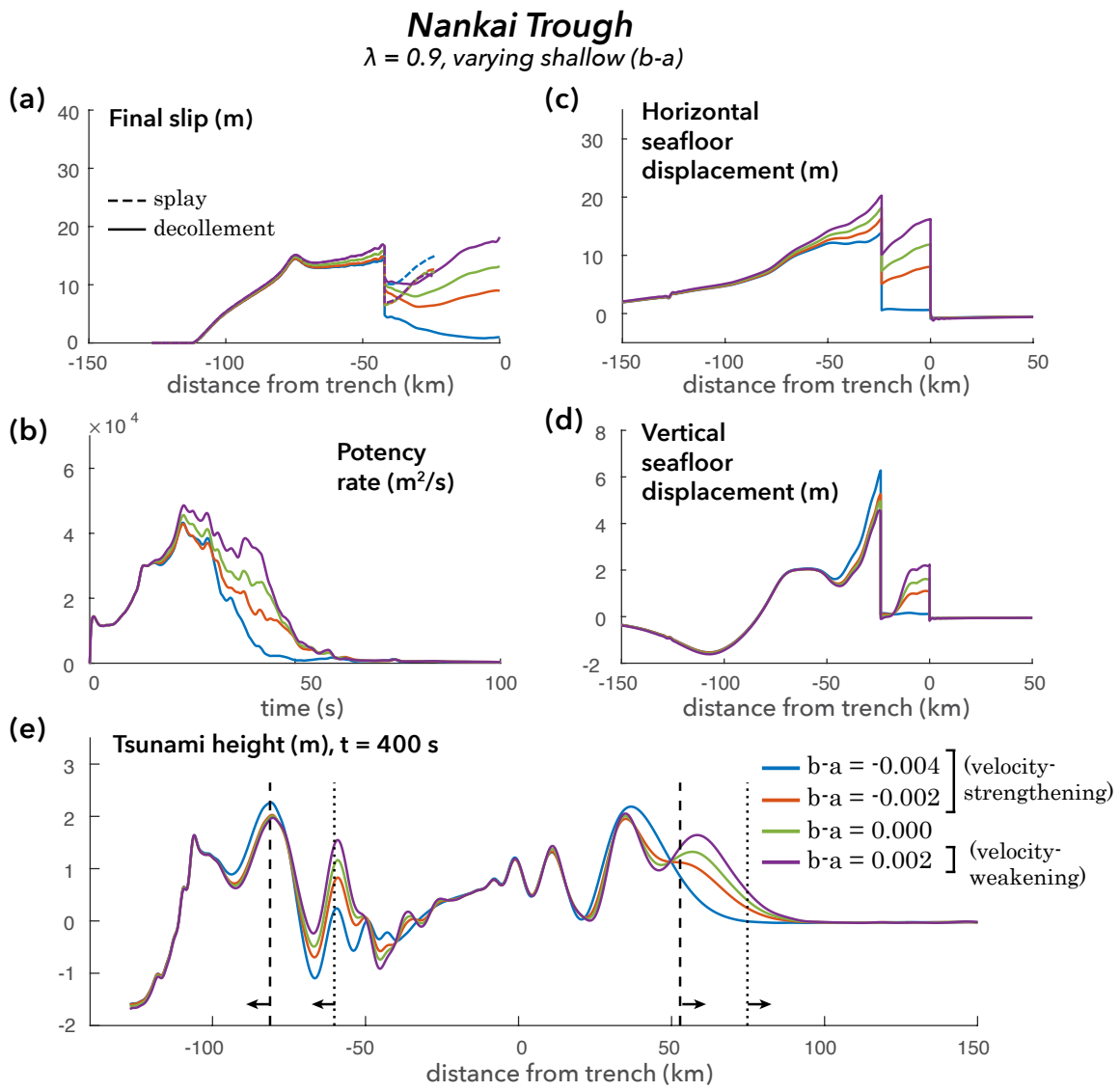

Fig. 8 Modeling results from the Nankai Trough, keeping pore pressure ratio constant at $\lambda = 0.9$ and varying $b - a$ identically on both the splay and décollement. Plots show (a) final slip on the splay and décollement, (b) potency rate of the earthquake, (c) horizontal and (d) vertical seafloor displacement at the final time step, with one peak each from motion on the splay and décollement, and (e) tsunami height at a time of $t = 400$ s. Vertical lines mark the distance the fastest tsunami waves produced at $x = 0$ (dotted) and $x = -23.8$ km (dashed) would travel by the final time step.

drop on the splay (see Supplementary Figure 22). The other three choices of $b - a$ all produce about the same slip on the splay, but, unsurprisingly, the more velocity-weakening models produce greater slip on the décollement. Interestingly, all four simulations result in slip along the splay, and that slip is greater at the seafloor than at the fault junction. Potency rate (Figure 8b)—defined in equations (7) and (8) and summed over both the splay and décollement—shows that ruptures that continue along the décollement produce more slip for longer periods of time than ruptures with less slip at the trench.

Slip is directly responsible for horizontal and vertical seafloor deformation (Figure 8c and d). Displacements peak at $x = 0$ and $x = -23.8$ km, where the décollement and splay reach the seafloor. Both peaks in vertical displacement correlate strongly with the shallow slip on the splay and décollement faults, with the $b - a = -0.004$ model causing maximum displacement on the splay peak and the $b - a = 0.002$ model topping the décollement peak. The splay peak sees greater displacement due to the higher angle of the splay fault compared to the décollement. The left-most peak in horizontal seafloor displacement, however, is strictly greater for models with more velocity-weakening friction.

In other words, models with greater $b-a$ more efficiently produce horizontal deformation even with less slip along the splay.

When the seafloor is sloping, as it does in the subduction zones presented in this study, vertical and horizontal seafloor motion both directly contribute to tsunami generation. Tsunami height, which is plotted at a time of $t = 400$ s in Figure 8e, shows the influence of both factors. The seaward wave (on the right side) and the landward wave each have two peaks, one each associated with the splay and the décollement. The leading seaward wave is caused by slip at the trench, and thus it does not exist for the $b - a = -0.004$ model. The second seaward peak—the higher amplitude of the two—is caused by splay rupture, and is greatest for the model with the most velocity-strengthening friction. The landward tsunami (excluding the section where $x < -100$ km, which is a seaward-traveling byproduct of the unrealistic ocean "cliff" in our structural model) also has two major peaks. Unlike the seaward tsunami, the leading landward wave is larger due its association with the splay. The height of the secondary landward signal scales strongly with $b - a$.

We see several qualitative similarities for Nankai Trough simulations where pore pressure ratio is set to $\lambda = 0.7$ (Figure 9), instead of $\lambda = 0.9$ (Figure 8), though for $\lambda = 0.7$ the higher prestress leads to overall greater slip, seafloor displacements, and tsunami heights than for $\lambda = 0.9$. Fault displacement on the shallow décollement—and to a lesser extent on the deep plate boundary fault—scales strongly with shallow $b - a$, ranging from zero slip on the trench ($b - a = -0.004$) to nearly 40 m ($b - a = 0.002$). As with $\lambda = 0.9$, we see that the model with the most velocity-strengthening friction actually produces the most slip on the splay, though the other models all produce some slip there as well. Models that slip to the trench produce secondary peaks in potency rate due to the greater length of the décollement and the extended slip amidst low-velocity sediments.

Once again, vertical and horizontal seafloor displacement features two main peaks, one each associated with the splay and the décollement. Horizontal displacement is everywhere greater with higher $b - a$. Vertical displacement around $x = 0$ similarly scales with $b - a$, but the $x = -23.8$ km peak is largest for $b - a = -0.004$ and virtually identical for the other three simulations. The resulting tsunami also shows two peaks traveling toward land and toward the sea. For all simulations except that with $b - a = 0.002$, the tsunami wave peak produced by the splay is the larger of the two, and therefore more important for hazard. The $b - a = -0.004$ simulation produces the highest and broadest splay peak, despite having the most velocity-strengthening friction.

Throughout this study, we have used structural models that are as realistic as possible, using constraints from seismic and drilling data. Such detailed structural models are rarely used in earthquake or tsunami studies, however. Here, we explore the full significance of the subduction zone structure by comparing the realistic structural model in Figure 6 to the two far simpler structural models in Figure 10d. Such compromises or simplifications to structure are commonly used, for example when converting fault slip to seafloor displacement using analytical solutions for dislocations in homogeneous half-spaces.

The first simplified structural model employs uniform material properties in the solid, using properties typical of rock fairly deep along the subducting plate (density $\rho = 2800$ kg/m^3, s-wave speed $\beta = 4$ km/s, and p-wave speed $\alpha = 7$ km/s). The second model simplified structural uses those values at all points deeper than approximately $y = -8.51$ km, the depth of the fault branch junction, and has values representative of shallow sediments ($\rho = 2.2$ kg/m^3, $\beta = 1.5$ km/s, and $\alpha = 3.1$ km/s) above that junction.

Figure 10 compares the results of using the three structural models on simulations where $\lambda = 0.9$ and $b-a = -0.002$ on both the splay and shallow décollement. For this set of plausible parameters, the two-layer structural model decreases the magnitude of slip and tsunami height, and reduces the maximum potency rate relative to the realistic, heterogeneous structural model. However, the uniform structural model fundamentally changes the character of the earthquake rupture. With the uniform model, all slip is confined to the splay, potency rate is consistently smoother and reveals a shorter rupture process, and the tsunami (excluding the nonphysical effects at $x < -100$ km) has a lower amplitude than either of the other two structural models.

7 Cascadia Subduction Zone - Background

The Cascadia Subduction zone is distinct from the Japan Trench and the Nankai Trough in that it has a relative absence of interplate seismicity over the historical record (e.g., [106, 107]). Still, great megathrust earthquakes are a known feature of the Cascadia margin over the past several millennia [112]. The most recent such event, inferred from evidence of coseismic subsidence in North America and an "orphan tsunami" in Japan, occurred

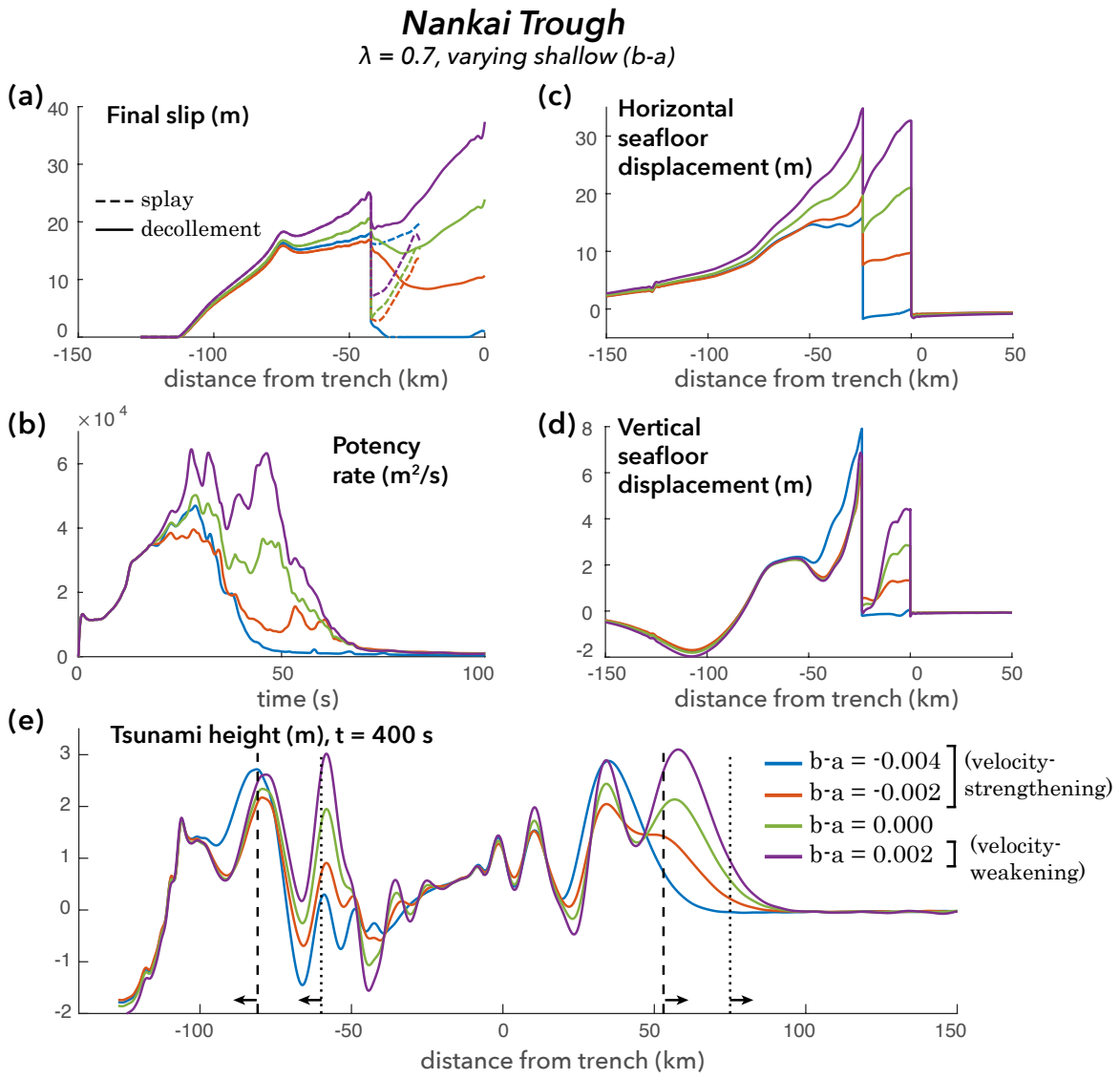

Fig. 9 Modeling results from the Nankai Trough, keeping pore pressure ratio constant at $\lambda = 0.7$ and varying $b - a$ identically on both the splay and décollement. Plots show (a) final slip on the splay and décollement, (b) potency rate of the earthquake, (c) horizontal and (d) vertical seafloor displacement at the final time step, with one peak each from motion on the splay and décollement, and (e) tsunami height at a time of $t = 400$ s. Vertical lines mark the distance the fastest tsunami waves produced at $x = 0$ (dotted) and $x = -23.8$ km (dashed) would travel by the final time.

on the evening of 26 January 1700 [63,79]. The approximately M_w 9.0 event was the latest in a series of full-margin ruptures that recur every 500-530 years (which, when combined with smaller events in southern Cascadia, leads to an average recurrence period of ∼240 years in that section) [20].

There have been few attempts to simulate dynamic earthquake rupture in the Cascadia Subduction Zone. Previous studies [14,47,80,107,108] have primarily used elastic dislocation models to estimate coseismic seafloor deformation and coastal subsidence given some prescribed fault slip. Those seafloor deformation calculations have sometimes been used to simulate tsunamis, although the process of converting earthquake slip to seafloor deformation to tsunami amplitude is not as straightforward as is often assumed for realistic earthquake scenarios [48]. The elastic dislocation models for Cascadia have been constrained mostly by evidence of coseismic subsidence from paleoseismic data, but also by thermal constraints, strain rate observations, and recurrence rates [107]. The growing paleoseismic evidence has for many years shown that at several locations along the Pacific Northwest coast, subsidence between 0.5 and 1.5 m occurred (e.g., [5, 21, 86]). More recent interpretations of subsidence data have confirmed the general magnitude of subsidence but inferred heterogeneous

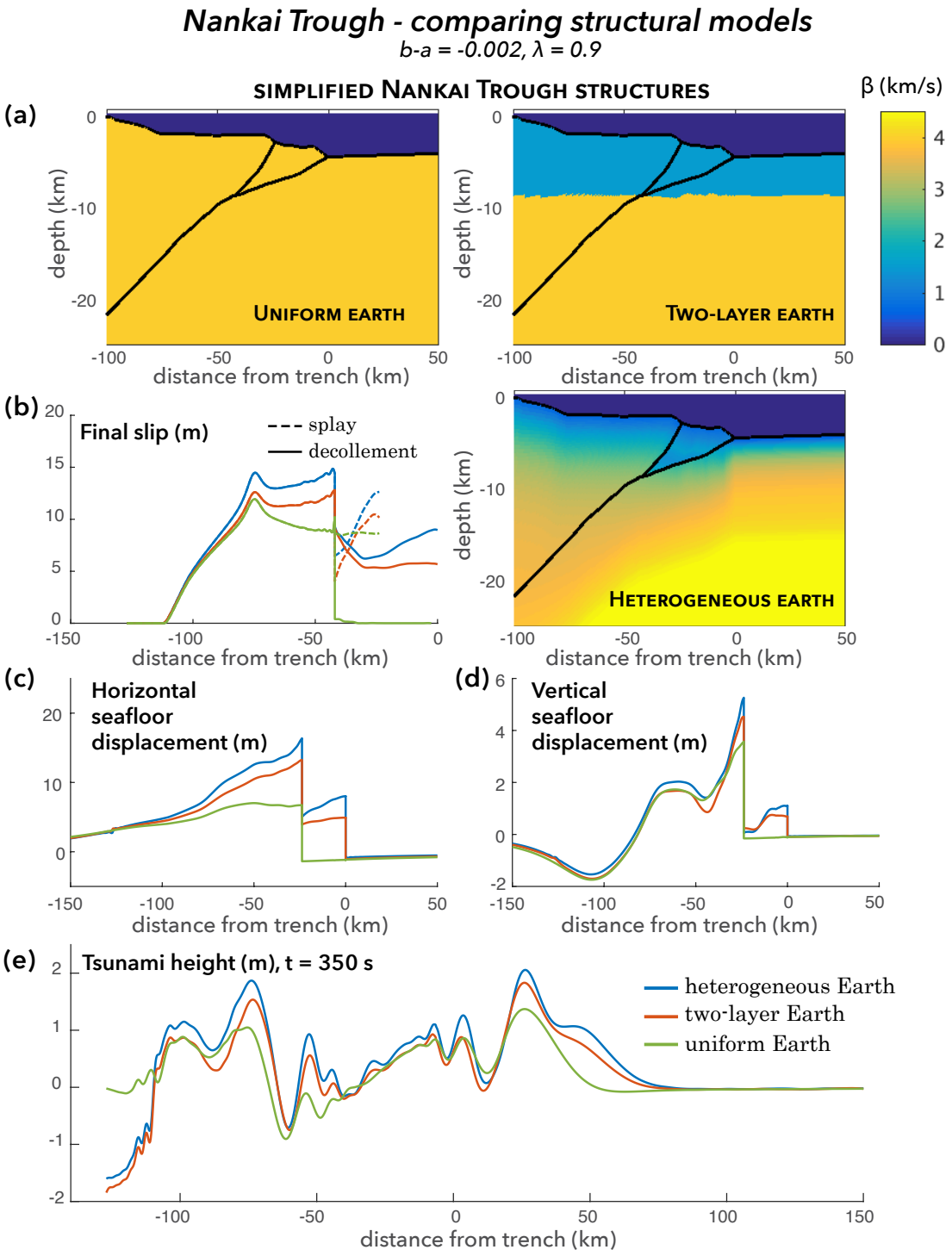

Fig. 10 Modeling results from the Nankai Trough with $\lambda = 0.9$ and $b - a = -0.002$ on both the splay and shallow décollement, comparing our standard realistic structural models to two simpler ones with (a) uniform material properties in the Earth and a two-layer set of material properties. Plots show (b) final slip on the splay and décollement, (c) horizontal and (d) vertical seafloor displacements, and (e) tsunami height at a time of $t = 350$ s.

slip along-strike for the 1700 event [37, 108], as is typical for recorded megathrust earthquakes. For the dislocation models, uncertainties in the subsidence data lead to a wide variety of acceptable slip models. And, crucially for tsunami hazard applications, coastal subsidence estimates carry no information to constrain shallow slip or tsunami height [108]. Earthquake rupture models that neither prescribe slip nor make too many assumptions about tsunami generation may prove useful for understanding local hazard in Cascadia.

Our 2D structural model draws on interpretations of two seismic transects: Line SO10 from the ORWELL Project [15] and Line 4 from the COAST dataset [24, 109]. The two seismic lines both cross the Cascadia margin just south of latitude 47°N, by Grays Harbor and Willapa Bay in Southwest Washington. Both profiles focus on the shallow portion of the subduction zone (depths less than 20 km), so we use the Juan de Fuca slab model of McCrory et al. [55] to inform the deeper geometry of our plate boundary fault.

Compared with the other subduction zones in this study and in the world, Cascadia is unique in terms of its structure and seismic quiescence [20,109]. Cascadia also has one of the hottest plate boundary thrusts, because of its young (∼8 Ma) subducting plate and thick incoming sediments; its high temperature may contribute to its dearth of interplate seismicity [54]. On the left side of our profile, there is a smooth, 2.5-3 km thick layer of undeformed sediments sitting above the oceanic crust. Starting at the deformation front (defined as $x = 0$), sediments form a large accretionary prism, whose outer wedge is interpreted to contain several landward vergent thrust faults [109] (though these have not been included in our simulations). The décollement in this section dips at an extremely shallow angle, less than 4°. A bathymetric feature known as the Quinault Ridge (at $x \approx 38$ km) separates the outer wedge from the lower slope terrace, or midslope terrace, where the prism continues to thicken. To the right of this section, starting at $x \approx 50$ km, is an older section of the accretionary prism. The continental shelf begins at $x \approx 76$ km, where a shallow layer of ocean (∼200 m depth) continues up to the coast, at $x = 142$ km. At its greatest depth, the ocean above the Cascadia margin is only 2.7 km deep, far shallower than the water above Nankai and the Japan Trench.

Neither seismic transect we use to build our Cascadia geometry shows evidence of a plate boundary thrust fault that breaches the seafloor at the deformation front. The lack of historic interplate earthquakes means that it is difficult to infer the rupture pathway at shallow depths. It is possible that the 1700 Cascadia earthquake ruptured to the trench, and elastic dislocation models that allow for trench-breaking rupture can sufficiently fit the subsidence data [108]. However, seeing no direct evidence of a décollement that meets the seafloor, we use a buried thrust fault in our simulations.

Prestress on the fault is set using the same procedure as in the Nankai Trough simulations. We calculate a depth-dependent pair of principal stresses σ_1 and σ_3 and project them onto the plate boundary thrust. The ratio of shear to normal stress projected on the fault allows us to estimate the friction coefficient f_0, which in this case is set to $f_0 = 0.2$ below the accretionary prism and linearly ramped up to 0.4 at the deepest part of the fault (Figure 3).

There is a good amount of evidence that the pore fluid along the fault is, as with Nankai and the Japan Trench, highly overpressured. Shear stress on the Cascadia subduction fault has been shown to be very low from heat flow measurements and focal mechanism solutions, and near-lithostatic pore pressure in the fault zone has been deemed to be the cause [105]. Others have invoked near-lithostatic pore pressure, especially at depth, to explain high Vp/Vs ratios beneath southern Vancouver Island [4, 68]. Seno [85] gives a quantitative estimate for the pore pressure ratio as $\lambda = 0.93$ for Washington and $\lambda = 0.895$ for South Vancouver Island. Once again, we run two sets of simulations, one with $\lambda = 0.7$ and the other with $\lambda = 0.9$.

We vary the shallow rate-and-state friction parameter $b - a$ in the same way we do for the Japan Trench, running various simulations with $b - a = -0.004, -0.002, 0.000$, or 0.002 under the accretionary prism, and $b - a = 0.004$ at depth (Figure 3).

8 Cascadia Subduction Zone - Results

The Cascadia Subduction Zone is the only one in our study with a completely buried plate boundary thrust. Its rupture behavior is, in many ways, much simpler than that of the Japan Trench or Nankai Trough, because it neither encounters a junction nor breaches the seafloor. However, we find that tsunamis generated in Cascadia have a surprisingly complex signal and source.

In Figure 12, we feature a set of Cascadia simulations with pore pressure ratio $\lambda = 0.9$, with shallow rate-and-state parameter $b - a$ varied between $b - a = -0.004$ and $b - a = 0.002$. Though we only plot the results with $\lambda = 0.9$, simulations with $\lambda = 0.7$ produce qualitatively similar results but with greater slip (30-80% more for models with $\lambda = 0.7$), tsunami heights, etc. As ex-

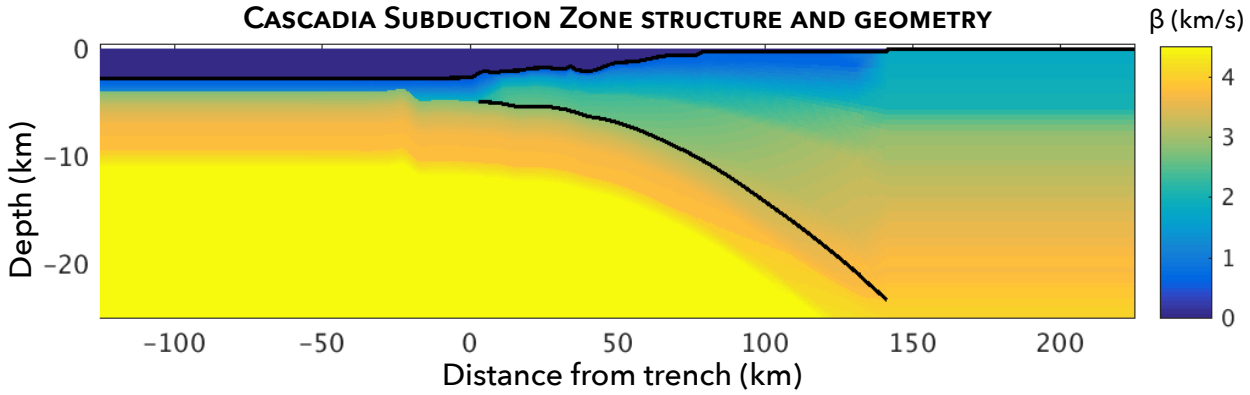

Fig. 11 Material structure and geometry of the Cascadia Subduction Zone used for our simulations, colored by shear wave speed β. Bold black lines trace the plate boundary fault and the seafloor.

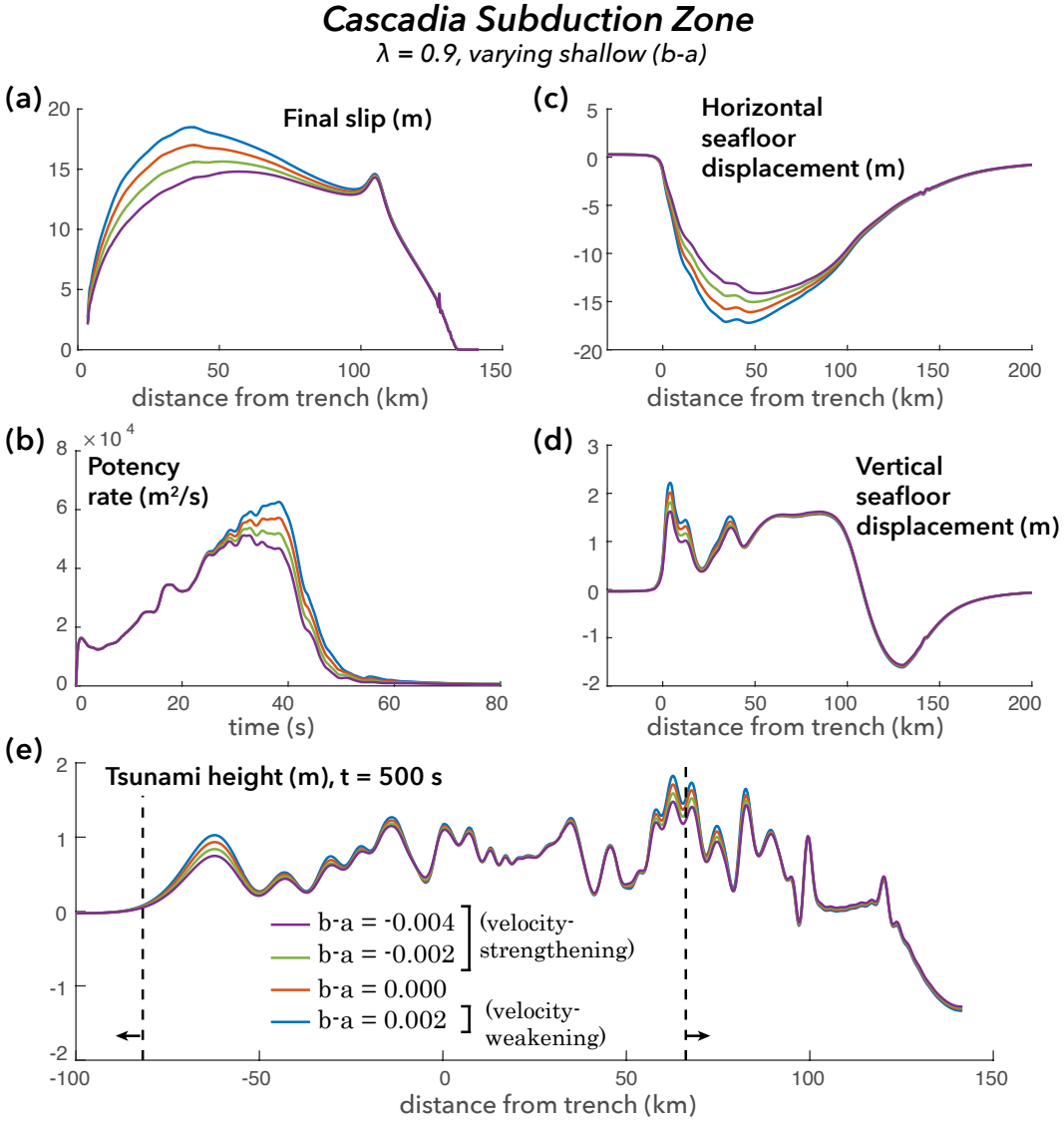

Fig. 12 Modeling results from the Cascadia Subduction Zone, keeping pore pressure ratio constant at $\lambda = 0.9$ and varying $b - a$ identically on both the splay and décollement. Plots show (a) final slip on the splay and décollement, (b) potency rate of the earthquake, (c) horizontal and (d) vertical seafloor displacement at the final time step, and (e) tsunami height at a time of $t = 500$ s. Vertical dashed lines mark the distance the fastest tsunami waves produced at $x = 0$ would travel by the final time step.

pected, the more velocity-weakening models experience greater stress drop (Supplementary Figure 23) and yield greater overall slip, especially in the region where $b - a$ varies ($x < 50$ km, as per the upper right plot of Figure 3). Cumulative slip is independent of shallow friction at the deepest and shallowest sections of the fault. Potency rate has a very similar history between simulations; the earthquake behaves in a qualitatively similar manner regardless of shallow $b - a$.

Horizontal seafloor displacement (Figure 12c) scales very clearly with slip, and shows a dependence on shallow $b - a$ for the region where $0 < x < 100$ km. Vertical seafloor displacement, however, shows the effects of varying slip to a lesser degree and in a more limited region, $x < 50$ km, with a maximum near $x = 0$ where the fault is closest to the surface. The final tsunami profile is more complex than those from the other two subduction zones due to the shallow depth of much of the fault slip and the roughness of the seafloor bathymetry. The details of the tsunami process will be discussed further in the next section, but here we note that the differences in the tsunami profiles between the various models in Figure 12e stem from differences in shallow slip and vertical seafloor displacement.

9 Comparison of Subduction Zones

The three subduction zones we focus on in this study show great variation in their geologic structure, seafloor bathymetry, and fault geometry. Thus far we have compared differences in results within each individual subduction zone, but in this section we make some comparisons across subduction zones. For each one, we select one reasonable parameter set and explore how unique features of each subduction zone influence earthquake rupture and tsunami generation and propagation. For the Japan Trench, we use the case with $\lambda = 0.9, f_0 = 0.35,$ and $b - a = -0.002$; for Nankai, we use $\lambda = 0.9$ and $b - a = -0.002$; and for Cascadia we use $\lambda = 0.9$ and $b - a = 0.000$.

9.1 Rupture Process

At each subduction zone, earthquake rupture begins with nucleation at depth and proceeds in both updip and downdip directions. Supplementary Figure 24 shows potency rate functions for the three subduction zones on the same plot, giving a relative sense of the time history of each rupture.

The Japan Trench rupture proceeds in a very similar way to that of the ruptures in our prior study of idealized subduction zones with compliant prisms [50]. We see in Figure 13a that rupture velocity gradually increases as the rupture propagates toward the trench then slows as it reaches the accretionary prism. There, slip velocity accelerates despite friction becoming more velocity-strengthening at the trench, leaving enhanced slip profiles like those of Figure 5a. This is caused by interactions with the seafloor and free surface and wave energy being trapped within the compliant prism.

In the Cascadia Subduction Zone (Figure 13b), rupture propagates more smoothly. As the earthquake travels updip, through moderately compliant materials but not through extremely weak sediments, slip velocity gradually increases around the rupture front. Since we do not allow rupture to continue up to the seafloor, the slip velocity does not increase explosively and rupture ceases near the deformation front, causing only limited reflection of slip downdip.

For the Nankai Trough, we visualize slip separately for the splay fault and the décollement. Downdip of $x = -42$ km, the junction between the splay and décollement, Figure 13c and d are identical because they show the same fault segment. Though not all Nankai simulations result in identical patterns of slip on the splay and décollement, the case shown here is typical in that rupture first continues to propagate along the décollement but later jumps to the middle of the splay fault. Slip on the décollement is patchier than it is for the other subduction zones. Slip on the splay tends to proceed from the middle outward, increasing at the trench but slipping less near the junction, leading to the final slip pattern shown in dashed lines in Figure 8.

9.2 Tsunami Generation and Propagation

One of the primary benefits of modeling subduction zone earthquakes and tsunamis in a fully coupled framework is the ability to observe the entire tsunami generation process without relying on various approximations typically used to convert seafloor displacement to tsunami initial conditions. Whereas typical tsunami models must convert seafloor displacements to sea surface height before running a tsunami simulation, our approach takes into account the full physics of the problem, including any possible contributions from momentum transfer between the Earth and ocean [48,89]. In this section, we track the entire tsunami process from generation to propagation, and compare between the three subduction zones of interest.

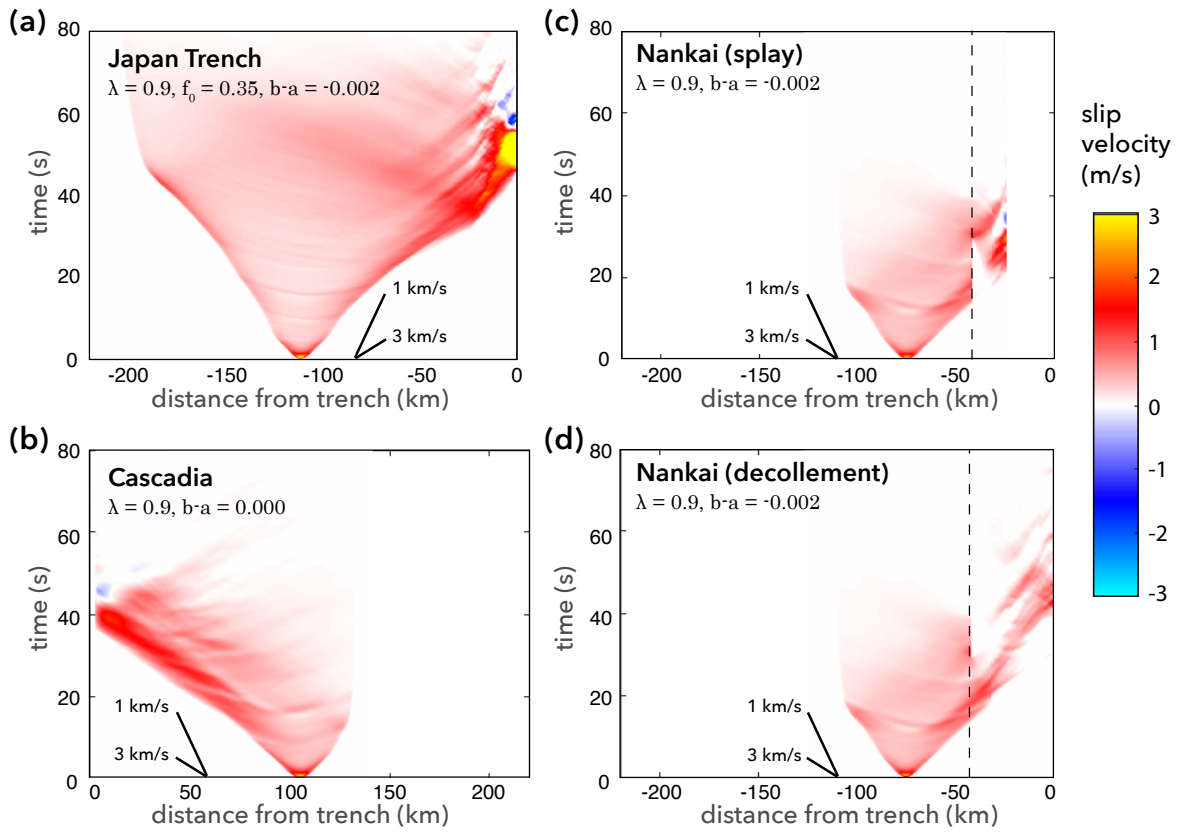

Fig. 13 Slip velocity over time and space for selected simulations on the following subduction zone faults: (a) Japan Trench, (b) Cascadia Subduction Zone, (c) Nankai Trough including the splay, and (d) Nankai including the décollement. Vertical dashed lines indicate location of splay-décollement junction.

In Figure 14 we plot the whole life cycle of a Japan Trench tsunami, for a simulation with parameters $\lambda = 0.9$, $f_0 = 0.35$ and shallow $b - a = -0.002$. Figure 14a shows the sea surface height at time $t = 500$ s, as in Figure 5e. This tsunami profile is the final slice of the space-time plot of sea surface height (Figure 14b). Earthquake nucleation occurs at about $x = -110$ km at time $t = 0$, with subsequent fault slip generating various guided waves including oceanic Rayleigh waves and leaking P-wave modes (or oceanic PL waves) [44] that are apparent on the ocean surface. The rupture continues to the trench at $x = 0$, where shallow slip leads directly to seafloor deformation, causing the beginnings of a tsunami at around $t = 50$ s. Rupture to the trench generates additional ocean-guided waves, especially in the seaward direction due to directivity. Since they travel at speeds much greater than the surface gravity wave speed, the tsunami emerges as a distinct feature by $t \approx 200$ s. The tsunami propagates dispersively until the end of the simulation. In this plot we also observe a tsunami wave caused by the horizontal motion of the nonphysical coastal "cliff" at $x = -220$ km, mentioned in previous sections and visible in the bathymetry profile of Figure 14d.

It is not possible to visualize a true initial condition on sea surface height; seafloor deformation occurs over tens of seconds and continuously excites surface gravity waves. Those waves begin to propagate even as the seafloor continues to deform. Furthermore, the dynamic nature of the tsunami generation process means that the initial tsunami waveform is superimposed with ocean acoustic waves, guided Rayleigh waves, oceanic PL waves, and other seismic waves. In Figure 14c we show two approaches to estimate the "initial" tsunami height. The first approach is to calculate the Tanioka and Satake initial condition on sea surface height, η_{ts}, from equation (1) using the static seafloor displacement. We plot the total $\eta_{ts}(x)$ as well as the separate contributions from vertical and horizontal displacement, $u_y(x)$ and $-m(x)u_x(x)$. The Tanioka and Satake initial condition considers neither nonhydrostatic effects nor the time-dependent rupture process, and therefore is a very simple interpretation of the initial tsunami. But it does yield an understanding of the relative importance of vertical and horizontal seafloor deformation.

The second approach involves running an identical simulation but with gravitational acceleration set to zero, i.e., $g = 0$. The zero gravity simulation

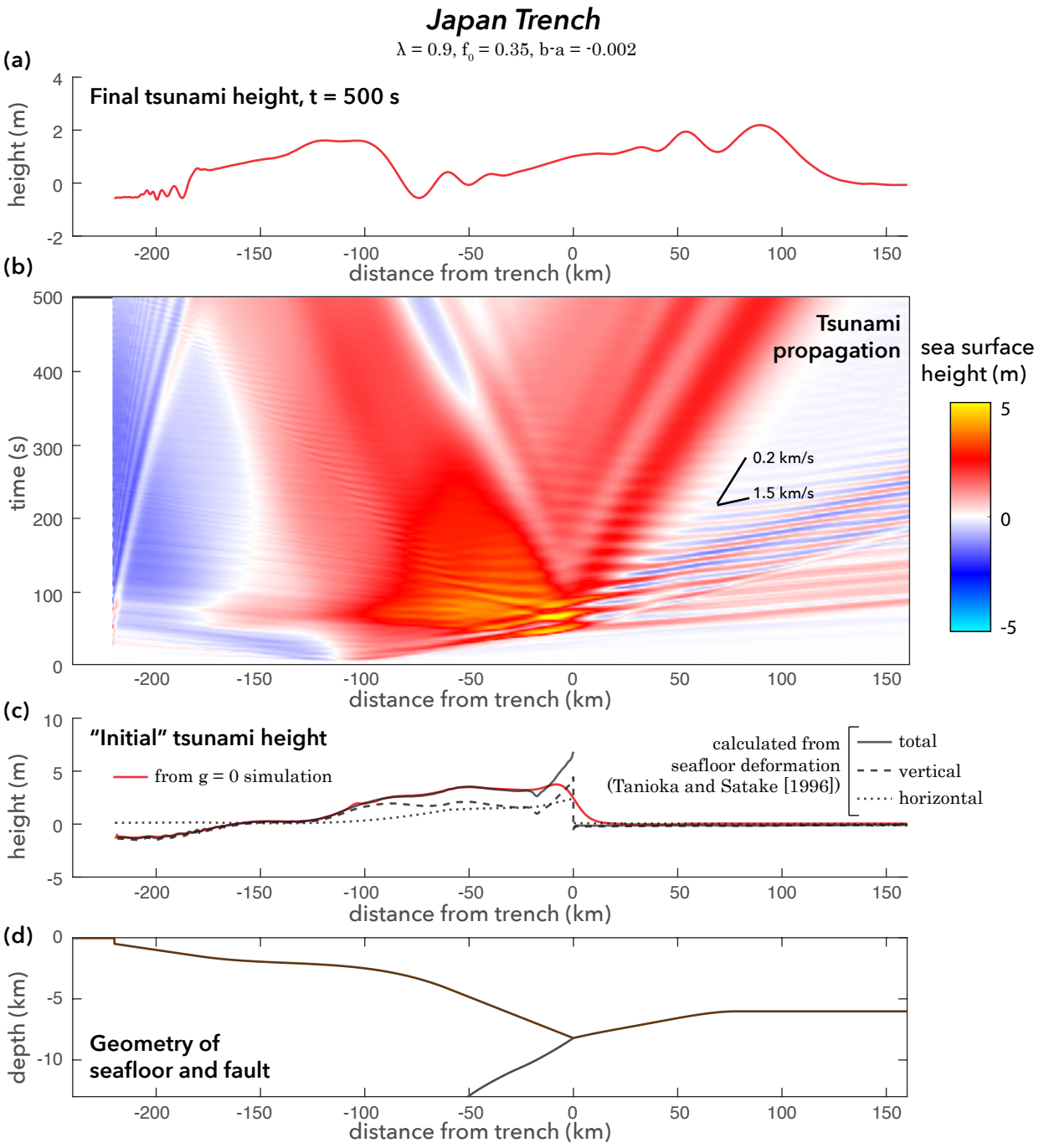

Fig. 14 The life cycle of a tsunami in the Japan Trench: (a) tsunami height at the final time step; (b) sea surface height, reflecting earthquake rupture from nucleation to the trench as well as tsunami propagation; (c) two estimates of initial tsunami height, one from a zero gravity simulation and another calculated from horizontal and vertical seafloor displacements; and (d) geometry of the seafloor and fault, which help determine seafloor motion.

results in a static sea surface perturbation, η_{zg}, that captures contributions from both vertical and horizontal displacements of the seafloor as well as the nonhydrostatic response of the ocean [33]; it is as close as possible to an initial condition for the tsunami.

We see that vertical and horizontal displacements both play a substantial role in generating the tsunami at the Japan Trench. The horizontal contribution, $-mu_x$, increases gradually from $x \approx -100$ km to the trench, while the vertical contribution, u_y, is about level until $x \approx -20$ km, where it dips a bit before peaking at the trench due to the influence of the compliant prism. We find that η_{zg} is nearly equivalent to η_{ts} except, notably, in the vicinity of the trench. The differences can be attributed to nonhydrostatic effects,

which effectively filter short wavelengths to make η_{zg} smoother than η_{ts}.

Figure 15 shows the life cycle of a tsunami in the Nankai Trough, for the simulation with $\lambda = 0.9$ and shallow $b - a = -0.002$. Figure 15a shows the final tsunami height, while Figure 15b shows the tsunami's progression from start to finish. For this set of parameters, we observe that the splay ($x \sim -25$ km) is the largest contributor to tsunami height, though slip on the décollement produces waves that manifest in the final tsunami height as an extension of the first seaward peak and in the second landward peak. Dispersion is clearly visible in the final tsunami profile between $x = -50$ km and $x = 25$ km. As with the Japan Trench, we observe oceanic Rayleigh waves and other guided waves traveling seaward.

The zero gravity sea surface profile, η_{zg}, shows the relative contributions of slip on the splay and décollement in the initial tsunami. (This plot would look substantially different for other Nankai simulations which have more or less slip on the décollement.) In the Nankai Trough, u_y plays a larger role in tsunami generation than $-mu_x$, except in the vicinity in the compliant prism and in the sloping area near the continental shelf, $-100 < x < 80$ km; much of the region between here and the surface expression of the splay is flat, i.e. $m \approx 0$. Also, as seen for the Japan Trench, nonhydrostatic ocean response at short wavelengths smooths η_{zg} relative to η_{ts}.

The tsunami in the Cascadia Subduction Zone (Figure 16) is more complex than that of either of the others, from start to finish. Rather than being dominated by one or two leading peaks traveling in opposite directions, the final tsunami profile is replete with many smaller peaks and troughs, arising from complexities in the seafloor bathymetry as well as dispersion during the subsequent propagation. The initial tsunami profile as determined from a zero gravity simulation shows at least seven small crests. Closer to the coast, where the fault rupture is deeper, the Tanioka and Satake initial condition η_{ts} closely parallels η_{zg}, but that match breaks down closer to the deformation front, where $x < 45$ km. A closer look at the components of η_{ts} reveals that most of the variations in the tsunami perturbation are due to horizontal deformation, and that vertical seafloor displacement is quite even.

Had we interpreted a smoother, more simplified version of the seafloor bathymetry, we would not observe such a complex tsunami profile. Some of the peaks in Figure 16(a) might not be present in a real Cascadia tsunami due to along-strike variations in slip and seafloor bathymetry. Those variations would produce even more complexity in the tsunami signal, even though many of the features of our bathymetry profile are fairly coherent along the direction parallel to the coast.

In order to better understand the complexity of the Cascadia tsunami, we run an equivalent simulation using a simple form of the shallow water wave equations linearized about a state of rest, similar to our previous study [48]. The equations are written as $\partial\eta/\partial t + \partial(hv)/\partial x = 0$ and $\partial v/\partial t + g\partial\eta/\partial x = 0$, with ocean depth h, sea surface height η, and depth-averaged horizontal velocity v. The water is inviscid and incompressible; advection, nonlinearity, and bottom friction are neglected. The latter processes become relevant near shore and during inundation, but the approximations are justified given our focus on tsunami generation and offshore propagation. The shallow water equations require two initial conditions: one on initial sea surface height $\eta_0(x)$ and another on initial velocity $v_0(x)$. For the initial condition on sea surface height, we use $\eta_0(x) = \eta_{zg}$, the sea surface perturbation for the zero gravity simulation. We set $v_0(x) = 0$, as is typically assumed, though we revisit the question of appropriate initial conditions in the next section.

Figure 17 shows the propagation of the tsunami using the shallow water wave equations, as well as a comparison of the final "full physics" tsunami of Figure 16a to the best-matching time step of the shallow water solution. Due to the finite rupture process of the full physics model, the shallow water solver is initiated at $t = 52$ s; this provides the best match in solutions at $t = 500$ s. We see in Figure 17a that the two simulations have significant disagreements; even where peaks can be colocated they tend to differ from one another in amplitude. Comparing Figures 16b and 17b reveals that the differences are largely due to the absence of dispersion in the shallow water model and its presence in the full physics simulation. The finite rupture duration is also responsible for some of the disparities, although its effect is small because the tsunami does not travel very far in the ∼50 s source process.

9.3 Tsunami Initial Conditions

In this section we take a closer look at the initial conditions of the tsunamis in our study, using an adjoint wavefield procedure developed by Lotto et al. [48]. While there may be several advantages to using fully-coupled numerical methods to model earthquakes and tsunamis, shallow water approaches tend to be far more computationally efficient and are therefore widely used by

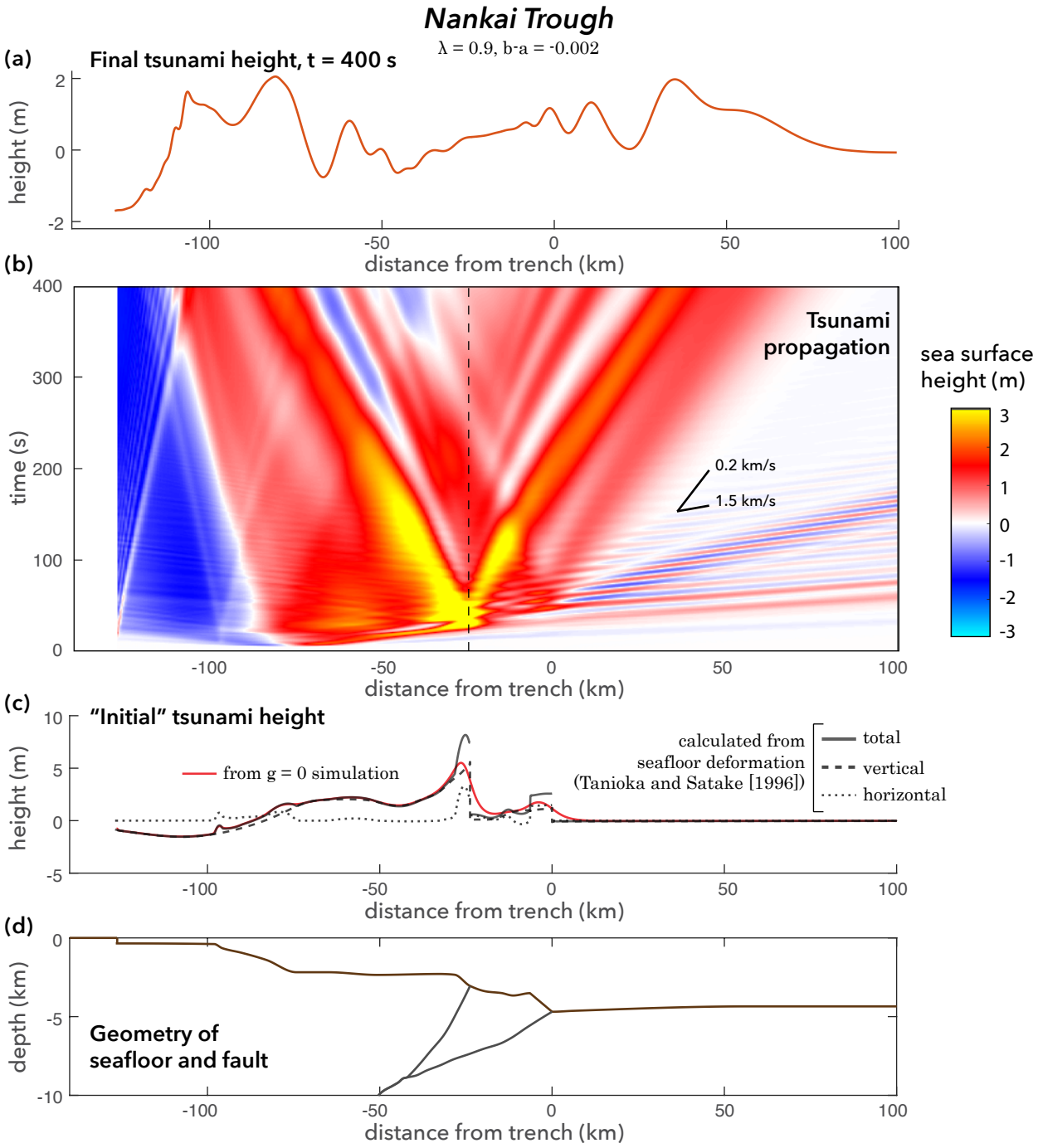

Fig. 15 The life cycle of a tsunami in the Nankai Trough: (a) tsunami height at the final time step; (b) sea surface height, reflecting earthquake rupture from nucleation to the trench as well as tsunami propagation; (c) two estimates of initial tsunami height, one from a zero gravity simulation and another calculated from horizontal and vertical seafloor displacements; and (d) geometry of the seafloor and faults, which help determine seafloor motion. Vertical dashed line marks where the splay intersects the seafloor.

the tsunami modeling community. Still, it is important to justify our assumptions with regard to tsunami initial conditions. Song and collaborators (e.g. [89, 90]) have argued that horizontal momentum transfer from the Earth to the ocean requires the use of a nonzero initial condition on depth-averaged horizontal velocity, v_0, but virtually all other studies assume $v_0 = 0$. In our previous work [48] we demonstrated that $v_0 = 0$ is the optimal initial condition for subduction zone earthquakes, though we largely studied a simplified subduction zone geometry. Here, we extend our previous work but with more realistic subduction zone geometries.

To generate self-consistent initial conditions for the Japan Trench, Nankai, and Cascadia, we begin

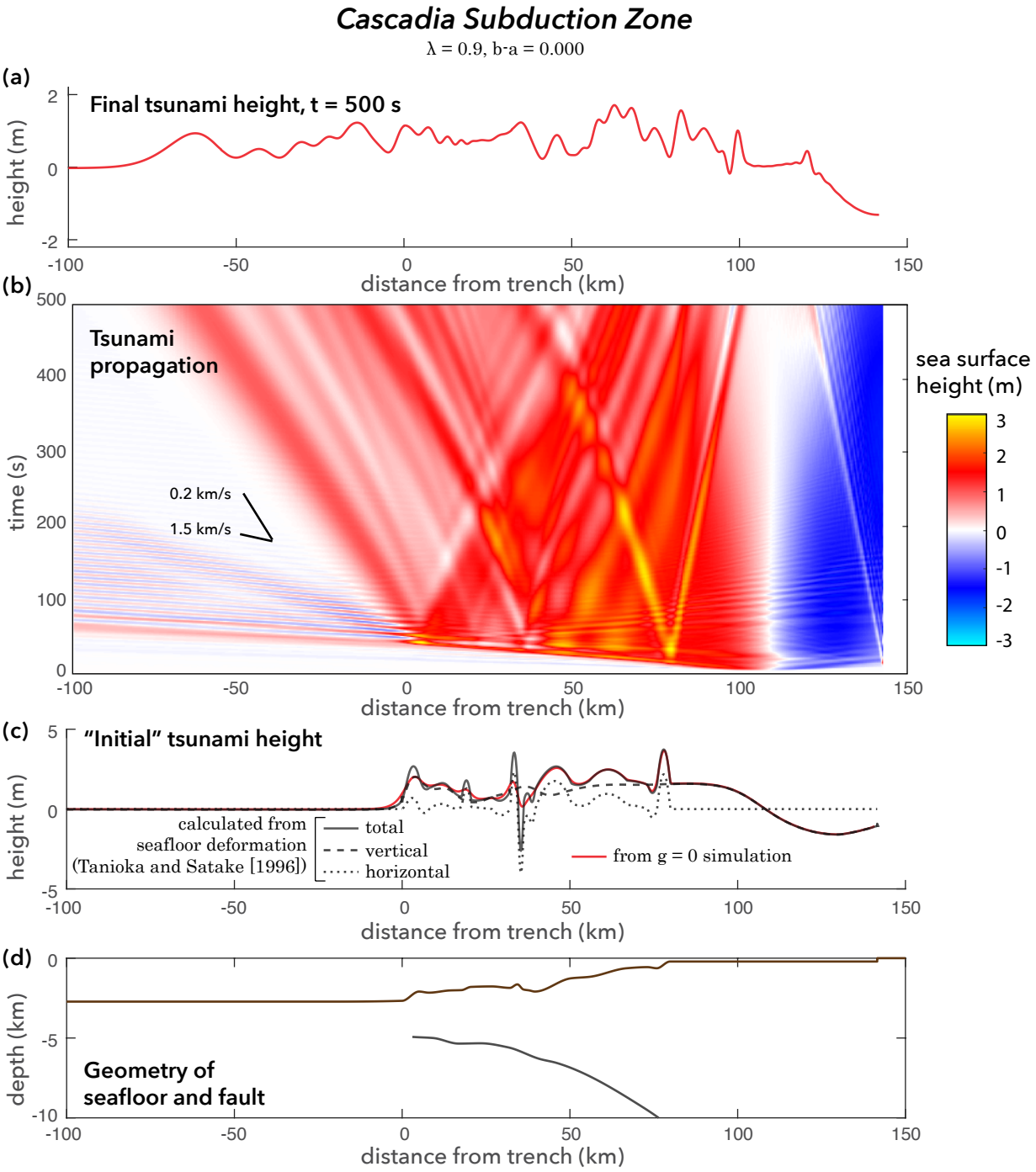

Fig. 16 The life cycle of a tsunami in the Cascadia Subduction Zone: (a) tsunami height at the final time step; (b) sea surface height, reflecting earthquake rupture from nucleation to the trench as well as tsunami propagation; (c) two estimates of initial tsunami height, one from a zero gravity simulation and another calculated from horizontal and vertical seafloor displacements; and (d) geometry of the seafloor and fault, which help determine seafloor motion.

by running a full-physics simulation to some final time where all seismic and ocean acoustic waves have left the computational domain, leaving only the slower-traveling tsunami. We then use the resulting stress and velocity fields as an initial condition on a time-reversed adjoint simulation, which involves simply flipping the sign of the particle velocity. We continue to use absorbing boundaries on the sides and bottom of the computational domain, and the waves that have left the domain are not re-injected in the adjoint problem. The governing equations are self-adjoint, so running it backward in time requires no additional changes to the code. The tsunami waves propagate backward in time toward the center of the domain where they converge above the earthquake source region, unper-

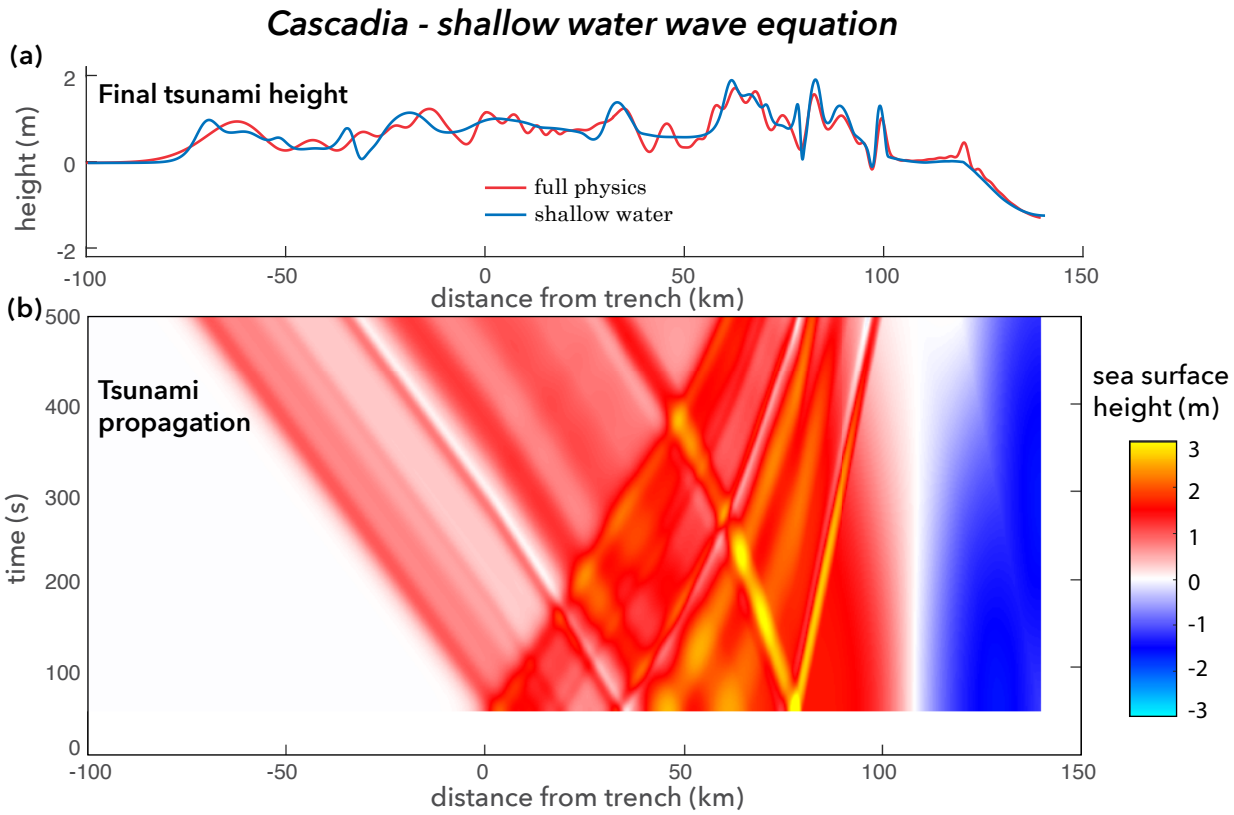

Fig. 17 The Cascadia tsunami modeled using the shallow water wave equations, using η_{zg} as an initial condition on tsunami height. (a) A comparison with the final tsunami profile from the equivalent full physics simulation. (b) A time-space plot of sea surface height, showing dispersion-free tsunami propagation using the shallow water wave equations.

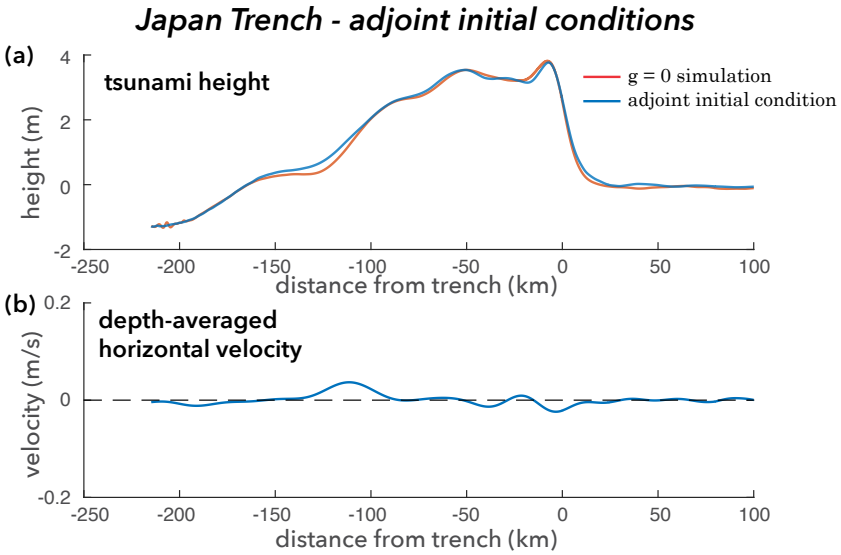

Fig. 18 Initial conditions determined from the adjoint (time-reversed) wave propagation problem for the Japan Trench. The tsunami initial conditions occur at a time equivalent to $t = 61$ s. (a) Initial tsunami height compared to the final sea surface height of the zero gravity simulation, η_{zg}. (b) Initial depth-averaged horizontal velocity.

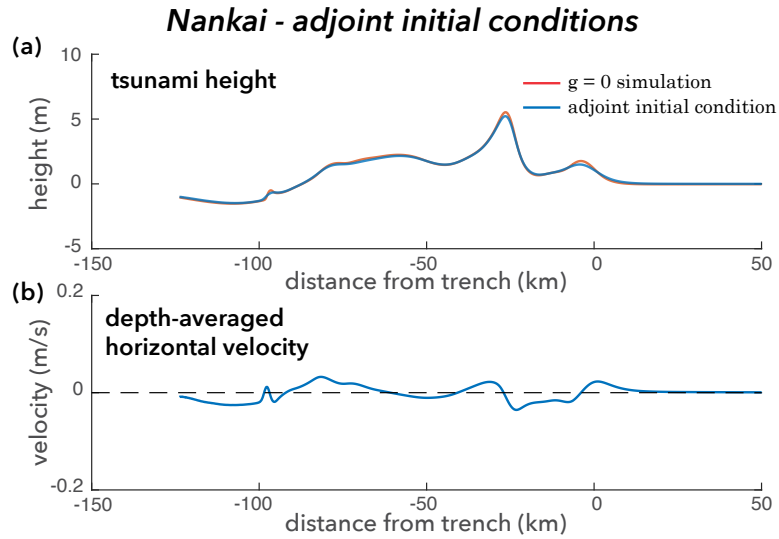

Fig. 19 Initial conditions determined from the adjoint (time-reversed) wave propagation problem for the Nankai Trough. The tsunami initial conditions occur at a time equivalent to $t = 32$ s. (a) Initial tsunami height compared to the final sea surface height of the zero gravity simulation, η_{zg}. (b) Initial depth-averaged horizontal velocity.

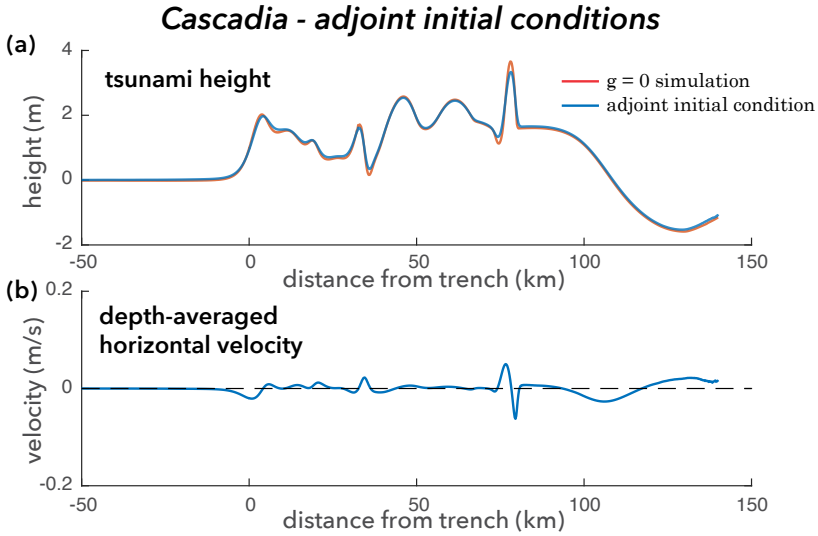

Fig. 20 Initial conditions determined from the adjoint (time-reversed) wave propagation problem for the Cascadia Subduction Zone. The tsunami initial conditions occur at a time equivalent to $t = 30$ s. (a) Initial tsunami height compared to the final sea surface height of the zero gravity simulation, η_{zg}. (b) Initial depth-averaged horizontal velocity.

turbed by seismic or acoustic waves as they were in the forward simulation. We choose as the initial condition the point when sea surface height most closely matches η_{zg} from the zero gravity simulation. To determine v_0, the initial condition on horizontal velocity, we take the average of horizontal particle velocity over the ocean depth.

For each of the three subduction zones (Figures 18, 19 and 20), we can find a time step in the time-reversed simulation that produces a tsunami closely matching η_{zg}. We observe that at the determined adjoint initial conditions, the tsunami from each subduction zone is associated with a small but nonzero horizontal velocity. The peaks in horizontal velocity may be loosely correlated with bathymetric features, although that relationship is difficult to distinguish. We used the results of the Cascadia adjoint simulation (with small, but nonzero v_0) as initial conditions for a shallow water simulation, as in Figure 17 which has $v_0 = 0$, and found only negligible differences between the two shallow water simulations. Thus, we conclude that the contribution of horizontal velocity to tsunami height is inconsequential.

10 Conclusions

Though most earthquake rupture models consider subduction zone geometries and structures that are idealized to a greater or lesser extent, there is much to be gleaned from making realistic choices about material properties and seafloor bathymetry.

In the Japan Trench, we have a classic subduction zone geometry, with a plate boundary fault dipping from the seafloor through a layer of sediments and a relatively small sedimentary prism all below a deep ocean layer. The presence of the compliant prism leads to enhanced slip and seafloor deformation near the trench, but this causes only a slight increase in tsunami height, given the small width of the prism ($\sim$20 km) relative to wavelengths filtered by the nonhydrostatic response of the ocean ($<\sim$ 40 km).

The presence of a prominent splay fault and a large and compliant sedimentary prism makes it hard to predict rupture pathway in the Nankai Trough. Some evidence suggests that rupture has occurred on the splay, and indeed all of our simulations show at least 10 m of slip at the splay fault tip. The magnitude of slip on the décollement is highly variable. Simulations with shallow highly velocity-strengthening friction result in almost zero décollement slip, whereas most others have slip on both fault segments. The splay poses the greater near-field hazard; motion on the splay more efficiently generates tsunami waves and those waves emanate from locations closer to shore, meaning that they will have the first and often greatest impact on human settlements.

The lack of a trench-breaking fault in our Cascadia model causes earthquakes and tsunamis to behave quite differently. Cascadia's thick sediment layer and gradually dipping plate boundary thrust, along with its rough bathymetry, lead to a complex tsunami signal. To the extent that its bathymetric ridges are coherent along strike we expect them to play a major role in tsunami generation, via the second term of equation (1). Even if they are not coherent along-strike, they will contribute to tsunami generation, but in an incoherent manner. Since the recent historic record includes no significant interplate seismicity in Cascadia, it is difficult to constrain the behavior of an tsunamigenic earthquake here. In a real event, thrust faults verging up from the décollement may be activated during a megathrust rupture, which could alter the pattern of shallow slip and thus the tsunami source.

In addition to focusing on individual subduction zones, we can make some general conclusions about the influence of friction, stress, and material structure on the earthquake rupture and tsunami generation process. Increases in prestress—including those due to decreases in pore pressure λ—consistently lead to increased fault displacement, seafloor motion, and tsunami height. The value of the rate-and-state parameter $b - a$ also has a major influence on shallow slip and tsunami heights. Not surprisingly, more velocity-strengthening friction usually leads to less slip, although in the Nankai case that relationship is complicated by the fact that changes in friction can lead the rupture to take entirely different pathways. Figure 10 demonstrates the effect of using realistic structural models on rupture pathway and tsunami height. Structural models with uniform material properties and models that only crudely employ compliant sediments tend to underestimate tsunami amplitudes.

Simulating realistic subduction models allows us to gain insights about tsunami physics and initial conditions for tsunami models decoupled from earthquake rupture. Running zero gravity simulations allows us to get a sense of initial tsunami height without interference from acoustic and seismic waves. By comparing sea surface profiles from those zero gravity simulations, η_{zg}, to the components of the Tanioka and Satake tsunami initial condition, η_{ts}, we observe that vertical and horizontal components of seafloor motion both contribute significantly to tsunami height. Neglecting contributions from horizontal seafloor displacement would cause one to underestimate tsunami height and qualitatively misrepresent the shape of the tsunami waveform.

But simply using η_{ts} as a tsunami initial condition would not be appropriate; the ocean's nonhydrostatic response smooths out the short wavelength variations in η_{ts}. This filtering effect, first described by Kajiura [33], accounts for the difference between η_{ts} and η_{zg} in Figures 14, 15, and 16. Ignoring the nonhydrostatic correction to η_{ts} would produce overly sharp peaks in the tsunami waveform.

What accounts for the differences between the tsunami of our full-physics model and that of the shallow water wave model in Figure 17? Space-time plots of sea surface height reveal that dispersion is responsible for much of the mismatches in the two profiles. To a lesser extent, the time-dependent rupture process of the full-physics model contributes disagreement, although in the cases studied it is acceptable to assume the tsunami does not travel sufficiently far over the tsunami source duration to require a time-dependent initial condition. The compressibility of the ocean in the full-physics model also has a negligible effect on tsunami propagation, echoing conclusions of much earlier

studies [84]. We also use an adjoint wave propagation method to run our full simulation backward in time, to produce initial tsunami conditions. The adjoint simulations demonstrate that, just as for the simplified geometry of our previous study [48], depth-averaged horizontal velocity in the ocean has a very small amplitude and hence a negligible effect on tsunami height for realistic subduction zone geometries.

Fully-coupled earthquake and tsunami codes can be difficult to implement and are more computationally expensive than methods that decouple the tsunami from its source process. However, coupled earthquake and tsunami simulations enable us to understand the details of subduction zone megathrust behavior and answer key questions about the physics of tsunami generation.

References

1. Michael Aldam, Shiqing Xu, Efim A Brener, Yehuda Ben-Zion, and Eran Bouchbinder. Nonmonotonicity of the frictional bimaterial effect. *Journal of Geophysical Research: Solid Earth*, 2017.
2. Masataka Ando. Source mechanisms and tectonic significance of historical earthquakes along the Nankai Trough, Japan. *Tectonophysics*, 27(2):119–140, 1975.
3. David J Andrews and Yehuda Ben-Zion. Wrinkle-like slip pulse on a fault between different materials. *Journal of Geophysical Research*, 102:553–571, 1997.
4. Pascal Audet, Michael G Bostock, Nikolas I Christensen, and Simon M Peacock. Seismic evidence for overpressured subducted oceanic crust and megathrust fault sealing. *Nature*, 457(7225):76, 2009.
5. Boyd E Benson, Brian F Atwater, David K Yamaguchi, Lorin J Amidon, Sarah L Brown, and Roger C Lewis. Renewal of tidal forests in Washington State after a subduction earthquake in AD 1700. *Quaternary Research*, 56(2):139–147, 2001.
6. Susan L Bilek and Thorne Lay. Rigidity variations with depth along interplate megathrust faults in subduction zones. *Nature*, 400(6743):443, 1999.
7. Michael L Blanpied, David A Lockner, and James D Byerlee. Frictional slip of granite at hydrothermal conditions. *Journal of Geophysical Research: Solid Earth*, 100(B7):13045–13064, 1995.
8. Richard W Briggs, Kerry Sieh, Aron J Meltzner, Danny Natawidjaja, John Galetzka, Bambang Suwargadi, Ya-ju Hsu, Mark Simons, Nugroho Hananto, Imam Suprihanto, et al. Deformation and slip along the Sunda megathrust in the great 2005 Nias-Simeulue earthquake. *Science*, 311(5769):1897–1901, 2006.
9. Frederick M Chester, Christie Rowe, Kohtaro Ujiie, James Kirkpatrick, Christine Regalla, Francesca Remitti, J Casey Moore, Virginia Toy, Monica Wolfson-Schwehr, Santanu Bose, et al. Structure and composition of the plate-boundary slip zone for the 2011 Tohoku-Oki earthquake. *Science*, 342(6163):1208–1211, 2013.
10. M Cocco and JR Rice. Pore pressure and poroelasticity effects in Coulomb stress analysis of earthquake interactions. *Journal of Geophysical Research: Solid Earth*, 107(B2), 2002.
11. Phil R Cummins and Yoshiyuki Kaneda. Possible splay fault slip during the 1946 Nankai earthquake. *Geophysical Research Letters*, 27(17):2725–2728, 2000.
12. Nora DeDontney and Judith Hubbard. Applying wedge theory to dynamic rupture modeling of fault junctions. *Bulletin of the Seismological Society of America*, 102(4):1693–1711, 2012.
13. Sean W Fleming and Anne M Tréhu. Crustal structure beneath the central Oregon convergent margin from potential-field modeling: Evidence for a buried basement ridge in local contact with a seaward dipping backstop. *Journal of Geophysical Research: Solid Earth*, 104(B9):20431–20447, 1999.
14. Paul Flück, RD Hyndman, and Kelin Wang. Three-dimensional dislocation model for great earthquakes of the Cascadia subduction zone. *Journal of Geophysical Research: Solid Earth*, 102(B9):20539–20550, 1997.
15. Ernst R Flueh, Michael A Fisher, Joerg Bialas, Jonathan R Childs, Dirk Klaeschen, Nina Kukowski, Tom Parsons, David W Scholl, Uri ten Brink, Anne M Tréhu, et al. New seismic images of the Cascadia subduction zone from cruise SO108—ORWELL. *Tectonophysics*, 293(1):69–84, 1998.
16. Y Fujii, K Satake, S Sakai, M Shinohara, and T Kanazawa. Tsunami source of the 2011 off the Pacific coast of Tohoku Earthquake. *Earth, planets and space*, 63(7):55, 2011.
17. Toshiya Fujiwara, Shuichi Kodaira, Yuka Kaiho, Narumi Takahashi, and Yoshiyuki Kaneda. The 2011 Tohoku-Oki earthquake: Displacement reaching the trench axis. *Science*, 334(6060):1240–1240, 2011.
18. PM Fulton, Emily E Brodsky, Y Kano, J Mori, F Chester, T Ishikawa, RN Harris, W Lin, Nobuhisa Eguchi, S Toczko, et al. Low coseismic friction on the Tohoku-Oki fault determined from temperature measurements. *Science*, 342(6163):1214–1217, 2013.
19. G L Gettemy and Harold J Tobin. Tectonic signatures in centimeter-scale velocity-porosity relationships of Costa Rica convergent margin sediments. *Journal of Geophysical Research: Solid Earth*, 108(B10), 2003.
20. Chris Goldfinger, C Hans Nelson, Ann E Morey, Joel E Johnson, Jason R Patton, Eugene Karabanov, Julia Gutierrez-Pastor, Andrew T Eriksson, Eulalia Gracia, Gita Dunhill, et al. Turbidite event history: Methods and implications for Holocene paleoseismicity of the Cascadia subduction zone. *US Geological Survey Professional Paper*, 1661:170, 2012.
21. Jean-Pierre Guilbault, John J Clague, and Martine Lapointe. Foraminiferal evidence for the amount of coseismic subsidence during a late Holocene earthquake on Vancouver Island, west coast of Canada. *Quaternary Science Reviews*, 15(8-9):913–937, 1996.
22. Sean PS Gulick, James A Austin Jr, Lisa C McNeill, Nathan LB Bangs, Kylara M Martin, Timothy J Henstock, Jonathan M Bull, Simon Dean, Yusuf S Djajadihardja, and Haryadi Permana. Updip rupture of the 2004 Sumatra earthquake extended by thick indurated sediments. *Nature Geoscience*, 4(7):453–456, 2011.

23. Tetsuro Hirono, Kenichi Tsuda, Wataru Tanikawa, Jean-Paul Ampuero, Bunichiro Shibazaki, Masataka Kinoshita, and James J Mori. Near-trench slip potential of megaquakes evaluated from fault properties and conditions. *Scientific reports*, 6:28184, 2016.
24. W Steven Holbrook, Graham Kent, Katie Keranen, H Paul Johnson, Anne Trehu, Harold Tobin, Jackie Caplan-Auerbach, and Jeff Beeson. Cascadia fore arc seismic survey: Open-access data available. *Eos, Transactions American Geophysical Union*, 93(50):521–522, 2012.
25. John Hower, Eric V Eslinger, Mark E Hower, and Edward A Perry. Mechanism of burial metamorphism of argillaceous sediment: 1. mineralogical and chemical evidence. *Geological Society of America Bulletin*, 87(5):725–737, 1976.
26. M K Hubbert and W W Rubey. Role of fluid pressure in mechanics of overthrust faulting: I. mechanics of fluid-filled porous solids and its application to overthrust faulting. *Geological Society of America Bulletin*, 70(2):115–166, 1959.
27. Robert D Hyndman and Kelin Wang. Thermal constraints on the zone of major thrust earthquake failure: The Cascadia subduction zone. *Journal of Geophysical Research: Solid Earth*, 98(B2):2039–2060, 1993.
28. Roy D Hyndman, Makoto Yamano, and Dan A Oleskevich. The seismogenic zone of subduction thrust faults. *Island Arc*, 6(3):244–260, 1997.
29. Matt J Ikari, Jun Kameda, Demian M Saffer, and Achim J Kopf. Strength characteristics of Japan Trench borehole samples in the high-slip region of the 2011 Tohoku-Oki earthquake. *Earth and Planetary Science Letters*, 412:35–41, 2015.
30. Matt J Ikari and Demian M Saffer. Comparison of frictional strength and velocity dependence between fault zones in the Nankai accretionary complex. *Geochemistry, Geophysics, Geosystems*, 12(4), 2011.
31. Scott Jennings and Graham R Thompson. Diagenesis of Plio-Pleistocene sediments of the Colorado River delta, southern California. *Journal of Sedimentary Research*, 56(1), 1986.
32. Tamara N Jeppson, Harold J Tobin, and Yoshitaka Hashimoto. Laboratory measurements quantifying elastic properties of accretionary wedge sediments: Implications for slip to the trench during the 2011 mw 9.0 tohoku-oki earthquake. *Geosphere*, 2018.
33. K Kajiura. The leading wave of a tsunami. *Bull. Earthq. Res. Inst.*, 43:535–571, 1963.
34. Nobuki Kame, James R Rice, and Renata Dmowska. Effects of prestress state and rupture velocity on dynamic fault branching. *Journal of Geophysical Research: Solid Earth*, 108(B5), 2003.
35. Rie Kamei, R Gerhard Pratt, and Takeshi Tsuji. Waveform tomography imaging of a megasplay fault system in the seismogenic Nankai subduction zone. *Earth and Planetary Science Letters*, 317:343–353, 2012.
36. Hiroo Kanamori and Masayuki Kikuchi. The 1992 Nicaragua earthquake: a slow tsunami earthquake associated with subducted sediments. *Nature*, 361(6414):714–716, 1993.
37. Andrew C Kemp, Niamh Cahill, Simon E Engelhart, Andrea D Hawkes, and Kelin Wang. Revising estimates of spatially variable subsidence during the ad 1700 Cascadia earthquake using a Bayesian foraminiferal transfer function. *Bulletin of the Seismological Society of America*, 108(2):654–673, 2018.
38. Masayuki Kikuchi, Misao Nakamura, and Kazumitsu Yoshikawa. Source rupture processes of the 1944 Tonankai earthquake and the 1945 Mikawa earthquake derived from low-gain seismograms. *Earth, Planets and Space*, 55(4):159–172, 2003.
39. Gaku Kimura, Shoko Hina, Yohei Hamada, Jun Kameda, Takeshi Tsuji, Masataka Kinoshita, and Asuka Yamaguchi. Runaway slip to the trench due to rupture of highly pressurized megathrust beneath the middle trench slope: The tsunamigenesis of the 2011 Tohoku earthquake off the east coast of northern Japan. *Earth and Planetary Science Letters*, 339:32–45, 2012.
40. Shuichi Kodaira, Tetsuo No, Yasuyuki Nakamura, Toshiya Fujiwara, Yuka Kaiho, Seiichi Miura, Narumi Takahashi, Yoshiyuki Kaneda, and Asahiko Taira. Coseismic fault rupture at the trench axis during the 2011 Tohoku-Oki earthquake. *Nature Geoscience*, 5(9):646–650, 2012.
41. Achim J Kopf and Kevin M Brown. Friction experiments on saturated sediments and their implications for the stress state of the Nankai and Barbados subduction thrusts. *Marine Geology*, 202(3):193–210, 2003.
42. H Kopp and N Kukowski. Backstop geometry and accretionary mechanics of the Sunda margin. *Tectonics*, 22(6), 2003.
43. JE Kozdon and EM Dunham. Rupture to the trench: Dynamic rupture simulations of the 11 March 2011 Tohoku earthquake. *Bull. Seism. Soc. Am.*, 103(2B):1275–1289, 2013.
44. JE Kozdon and EM Dunham. Constraining shallow slip and tsunami excitation in megathrust ruptures using seismic and ocean acoustic waves recorded on ocean-bottom sensor networks. *Earth and Planetary Science Letters*, 396:56–65, 2014.
45. Jeremy E Kozdon, Eric M Dunham, and Jan Nordström. Simulation of dynamic earthquake ruptures in complex geometries using high-order finite difference methods. *J. Sci. Comput.*, 55(1):92–124, 2013.
46. Thorne Lay, Charles J Ammon, Hiroo Kanamori, Yoshiki Yamazaki, Kwok Fai Cheung, and Alexander R Hutko. The 25 October 2010 Mentawai tsunami earthquake (Mw 7.8) and the tsunami hazard presented by shallow megathrust ruptures. *Geophysical Research Letters*, 38(6), 2011.
47. Lucinda J Leonard, Claire A Currie, Stéphane Mazzotti, and Roy D Hyndman. Rupture area and displacement of past Cascadia great earthquakes from coastal coseismic subsidence. *Bulletin*, 122(11-12):2079–2096, 2010.
48. Gabriel C Lotto, Gabriel Nava, and Eric M Dunham. Should tsunami simulations include a nonzero initial horizontal velocity? *Earth, Planets and Space*, 69(1):117, 2017.
49. GC Lotto and EM Dunham. High-order finite difference modeling of tsunami generation in a compressible ocean from offshore earthquakes. *Computational Geosciences*, 2015.
50. GC Lotto, EM Dunham, TN Jeppson, and HJ Tobin. The effect of compliant prisms on subduction zone earthquakes and tsunamis. *Earth and Planetary Science Letters*, 458:213–222, 2017.
51. Shuo Ma. A self-consistent mechanism for slow dynamic deformation and tsunami generation for earthquakes in the shallow subduction zone. *Geophysical Research Letters*, 39(11), 2012.
52. Shuo Ma and Gregory C Beroza. Rupture dynamics on a bimaterial interface for dipping faults.

Bulletin of the Seismological Society of America, 98(4):1642–1658, 2008.
53. T Maeda and T Furumura. FDM simulation of seismic waves, ocean acoustic waves, and tsunamis based on tsunami-coupled equations of motion. *Pure Appl. Geophys.*, 170(1-2):109–127, 2013.
54. Robert McCaffrey. Influences of recurrence times and fault zone temperatures on the age-rate dependence of subduction zone seismicity. *Journal of Geophysical Research: Solid Earth*, 102(B10):22839–22854, 1997.
55. Patricia A McCrory, J Luke Blair, Felix Waldhauser, and David H Oppenheimer. Juan de Fuca slab geometry and its relation to Wadati-Benioff zone seismicity. *Journal of Geophysical Research: Solid Earth*, 117(B9), 2012.
56. EK Mitchell, Y Fialko, and KM Brown. Frictional properties of gabbro at conditions corresponding to slow slip events in subduction zones. *Geochemistry, Geophysics, Geosystems*, 16(11):4006–4020, 2015.
57. Seiichi Miura, Narumi Takahashi, Ayako Nakanishi, Tetsuro Tsuru, Shuichi Kodaira, and Yoshiyuki Kaneda. Structural characteristics off Miyagi forearc region, the Japan Trench seismogenic zone, deduced from a wide-angle reflection and refraction study. *Tectonophysics*, 407(3):165–188, 2005.
58. GF Moore, NL Bangs, A Taira, S Kuramoto, E Pangborn, and HJ Tobin. Three-dimensional splay fault geometry and implications for tsunami generation. *Science*, 318(5853):1128–1131, 2007.
59. J Casey Moore and Peter Vrolijk. Fluids in accretionary prisms. *Reviews of Geophysics*, 30(2):113–135, 1992.
60. JJ Mori, FM Chester, N Eguchi, and S Toczko. Japan Trench Fast Earthquake Drilling Project (JFAST). *IODP Sci. Prosp*, 343(10.2204), 2012.
61. Yasuyuki Nakamura, Shuichi Kodaira, Becky J Cook, Tamara Jeppson, Takafumi Kasaya, Yojiro Yamamoto, Yoshitaka Hashimoto, Mika Yamaguchi, Koichiro Obana, and Gou Fujie. Seismic imaging and velocity structure around the JFAST drill site in the Japan Trench: low Vp, high Vp/Vs in the transparent frontal prism. *Earth, Planets and Space*, 66(1):1–12, 2014.
62. Ayako Nakanishi, Narumi Takahashi, Jin-Oh Park, Seiichi Miura, Shuichi Kodaira, Yoshiyuki Kaneda, Naoshi Hirata, Takaya Iwasaki, and Masao Nakamura. Crustal structure across the coseismic rupture zone of the 1944 Tonankai earthquake, the central Nankai Trough seismogenic zone. *Journal of Geophysical Research: Solid Earth*, 107(B1), 2002.
63. Alan R Nelson, Brian F Atwater, Peter T Bobrowsky, Lee-Ann Bradley, John J Clague, Gary A Carver, Mark E Darienzo, Wendy C Grant, Harold W Krueger, Rodger Sparks, et al. Radiocarbon evidence for extensive plate-boundary rupture about 300 years ago at the Cascadia subduction zone. *Nature*, 378(6555):371, 1995.
64. DA Oleskevich, RD Hyndman, and K Wang. The updip and downdip limits to great subduction earthquakes: Thermal and structural models of Cascadia, south Alaska, SW Japan, and Chile. *Journal of Geophysical Research: Solid Earth*, 104(B7):14965–14991, 1999.
65. Shinzaburo Ozawa, Takuya Nishimura, Hisashi Suito, Tomokazu Kobayashi, Mikio Tobita, and Tetsuro Imakiire. Coseismic and postseismic slip of the 2011 magnitude-9 Tohoku-Oki earthquake. *Nature*, 475(7356):373, 2011.
66. Jin-Oh Park, Tetsuro Tsuru, Shuichi Kodaira, Phil R Cummins, and Yoshiyuki Kaneda. Splay fault branching along the Nankai subduction zone. *Science*, 297(5584):1157–1160, 2002.
67. Jin-Oh Park, Tetsuro Tsuru, Narumi Takahashi, Takane Hori, Shuichi Kodaira, Ayako Nakanishi, Seiichi Miura, and Yoshiyuki Kaneda. A deep strong reflector in the Nankai accretionary wedge from multichannel seismic data: Implications for underplating and interseismic shear stress release. *Journal of Geophysical Research: Solid Earth*, 107(B4), 2002.
68. Simon M Peacock, Nikolas I Christensen, Michael G Bostock, and Pascal Audet. High pore pressures and porosity at 35 km depth in the Cascadia subduction zone. *Geology*, 39(5):471–474, 2011.
69. George Plafker. Alaskan earthquake of 1964 and Chilean earthquake of 1960: Implications for arc tectonics. *Journal of Geophysical Research*, 77(5):901–925, 1972.
70. Jascha Polet and Hiroo Kanamori. Shallow subduction zone earthquakes and their tsunamigenic potential. *Geophysical Journal International*, 142(3):684–702, 2000.
71. Hugues Raimbourg, Yozo Hamano, Saneatsu Saito, Masataka Kinoshita, and Achim Kopf. Acoustic and mechanical properties of Nankai accretionary prism core samples. *Geochemistry, Geophysics, Geosystems*, 12(4), 2011.
72. James R Rice. Fault stress states, pore pressure distributions, and the weakness of the San Andreas fault. In *International geophysics*, volume 51, pages 475–503. Elsevier, 1992.
73. Demian M Saffer and Chris Marone. Comparison of smectite-and illite-rich gouge frictional properties: application to the updip limit of the seismogenic zone along subduction megathrusts. *Earth and Planetary Science Letters*, 215(1):219–235, 2003.
74. Demian M Saffer and Harold J Tobin. Hydrogeology and mechanics of subduction zone forearcs: Fluid flow and pore pressure. *Annual Review of Earth and Planetary Sciences*, 39:157–186, 2011.
75. Takeshi Sagiya and Wayne Thatcher. Coseismic slip resolution along a plate boundary megathrust: The Nankai Trough, southwest Japan. *Journal of Geophysical Research: Solid Earth*, 104(B1):1111–1129, 1999.
76. Tatsuhiko Saito and Hiroaki Tsushima. Synthesizing ocean bottom pressure records including seismic wave and tsunami contributions: Toward realistic tests of monitoring systems. *Journal of Geophysical Research: Solid Earth*, 121(11):8175–8195, 2016.
77. Arito Sakaguchi, Frederick Chester, Daniel Curewitz, Olivier Fabbri, David Goldsby, Gaku Kimura, Chun-Feng Li, Yuka Masaki, Elizabeth J Screaton, Akito Tsutsumi, et al. Seismic slip propagation to the updip end of plate boundary subduction interface faults: Vitrinite reflectance geothermometry on Integrated Ocean Drilling Program NanTro SEIZE cores. *Geology*, 39(4):395–398, 2011.
78. Kenji Satake. Mechanism of the 1992 Nicaragua tsunami earthquake. *Geophysical Research Letters*, 21(23):2519–2522, 1994.
79. Kenji Satake, Kunihiko Shimazaki, Yoshinobu Tsuji, and Kazue Ueda. Time and size of a giant earthquake in Cascadia inferred from

Japanese tsunami records of January 1700. *Nature*, 379(6562):246–249, 1996.
80. Kenji Satake, Kelin Wang, and Brian F Atwater. Fault slip and seismic moment of the 1700 Cascadia earthquake inferred from Japanese tsunami descriptions. *Journal of Geophysical Research: Solid Earth*, 108(B11), 2003.
81. M Sato, T Ishikawa, N Ujihara, S Yoshida, M Fujita, M Mochizuki, and A Asada. Displacement above the hypocenter of the 2011 Tohoku-Oki earthquake. *Science*, 332(6036):1395–1395, 2011.
82. Michiyo Sawai, André R Niemeijer, Takehiro Hirose, and Christopher J Spiers. Frictional properties of JFAST core samples and implications for slow earthquakes at the Tohoku subduction zone. *Geophysical Research Letters*, 44(17):8822–8831, 2017.
83. Michiyo Sawai, André R Niemeijer, Oliver Plümper, Takehiro Hirose, and Christopher J Spiers. Nucleation of frictional instability caused by fluid pressurization in subducted blueschist. *Geophysical Research Letters*, 43(6):2543–2551, 2016.
84. Christopher Cedric Lytton Sells. The effect of a sudden change of shape of the bottom of a slightly compressible ocean. *Philos. Trans. R. Soc. Lond. Ser. A, Math. Phys. Sci.*, 258(1092):495–528, 1965.
85. Tetsuzo Seno. Determination of the pore fluid pressure ratio at seismogenic megathrusts in subduction zones: Implications for strength of asperities and Andean-type mountain building. *Journal of Geophysical Research: Solid Earth*, 114(B5), 2009.
86. I Shennan, AJ Long, MM Rutherford, FM Green, JB Innes, JM Lloyd, Y Zong, and KJ Walker. Tidal marsh stratigraphy, sea-level change and large earthquakes, i: a 5000 year record in Washington, USA. *Quaternary Science Reviews*, 15(10):1023–1059, 1996.
87. Thomas H Shipley, Kirk D McIntosh, Eli A Silver, and Paul L Stoffa. Three-dimensional seismic imaging of the Costa Rica accretionary prism: Structural diversity in a small volume of the lower slope. *Journal of Geophysical Research: Solid Earth*, 97(B4):4439–4459, 1992.
88. Robert M Skarbek and Demian M Saffer. Pore pressure development beneath the décollement at the Nankai subduction zone: Implications for plate boundary fault strength and sediment dewatering. *Journal of Geophysical Research: Solid Earth*, 114(B7), 2009.
89. YT Song, L-L Fu, V Zlotnicki, C Ji, V Hjorleifsdottir, CK Shum, and Y Yi. The role of horizontal impulses of the faulting continental slope in generating the 26 December 2004 tsunami. *Ocean Modelling*, 20(4):362–379, 2008.
90. YT Song, A Mohtat, and SC Yim. New insights on tsunami genesis and energy source. *Journal of Geophysical Research: Oceans*, 2017.
91. Seth Stein and Emile A Okal. Seismology: Speed and size of the Sumatra earthquake. *Nature*, 434(7033):581–582, 2005.
92. Shintaro Tamura and Satoshi Ide. Numerical study of splay faults in subduction zones: The effects of bimaterial interface and free surface. *Journal of Geophysical Research: Solid Earth*, 116(B10), 2011.
93. Y Tanioka and K Satake. Tsunami generation by horizontal displacement of ocean bottom. *Geophysical Research Letters*, 23(8):861–864, 1996.
94. Yuichiro Tanioka and Kenji Satake. Fault parameters of the 1896 Sanriku tsunami earthquake estimated from tsunami numerical modeling. *Geophysical Research Letters*, 23(13):1549–1552, 1996.
95. Yuichiro Tanioka and Kenji Satake. Coseismic slip distribution of the 1946 Nankai earthquake and aseismic slips caused by the earthquake. *Earth, planets and space*, 53(4):235–241, 2001.
96. Harold J Tobin and J Casey Moore. Variations in ultrasonic velocity and density with pore pressure in the decollement zone, northern Barbados Ridge accretionary prism. In *Proceedings of the Ocean Drilling Program. Scientific results*, pages 125–136. National Science Foundation, 1997.
97. Harold J Tobin, J Casey Moore, and GF Moore. Laboratory measurement of velocity vs. effective stress in thrust faults of the Oregon accretionary prism: Implications for fault zone overpressure. In *Proceedings of the Ocean Drilling Program. Scientific results*, volume 146, pages 349–358. Ocean Drilling Program, 1995.
98. Harold J Tobin and Demian M Saffer. Elevated fluid pressure and extreme mechanical weakness of a plate boundary thrust, Nankai Trough subduction zonerough subduction zone. *Geology*, 37(8):679–682, 2009.
99. Simon T Tse and James R Rice. Crustal earthquake instability in relation to the depth variation of frictional slip properties. *Journal of Geophysical Research: Solid Earth*, 91(B9):9452–9472, 1986.
100. Takeshi Tsuji, Rie Kamei, and R Gerhard Pratt. Pore pressure distribution of a mega-splay fault system in the Nankai Trough subduction zone: Insight into up-dip extent of the seismogenic zone. *Earth and Planetary Science Letters*, 396:165–178, 2014.
101. Kohtaro Ujiie, Hanae Tanaka, Tsubasa Saito, Akito Tsutsumi, James J Mori, Jun Kameda, Emily E Brodsky, Frederick M Chester, Nobuhisa Eguchi, Sean Toczko, et al. Low coseismic shear stress on the Tohoku-Oki megathrust determined from laboratory experiments. *Science*, 342(6163):1211–1214, 2013.
102. Roland von Huene, Cesar R Ranero, and Dave W Scholl. Convergent margin structure in high-quality geophysical images and current kinematic and dynamic models. In *Subduction Zone Geodynamics*, pages 137–157. Springer, 2009.
103. Chi-yuen Wang. Sediment subduction and frictional sliding in a subduction zone. *Geology*, 8(11):530–533, 1980.
104. Kelin Wang and Yan Hu. Accretionary prisms in subduction earthquake cycles: The theory of dynamic Coulomb wedge. *Journal of Geophysical Research: Solid Earth*, 111(B6), 2006.
105. Kelin Wang, Taimi Mulder, Garry C Rogers, and Roy D Hyndman. Case for very low coupling stress on the Cascadia Subduction Fault. *Journal of Geophysical Research: Solid Earth*, 100(B7):12907–12918, 1995.
106. Kelin Wang and Anne M Tréhu. Invited review paper: Some outstanding issues in the study of great megathrust earthquakes—The Cascadia example. *Journal of Geodynamics*, 98:1–18, 2016.
107. Kelin Wang, Ray Wells, Stephane Mazzotti, Roy D Hyndman, and Takeshi Sagiya. A revised dislocation model of interseismic deformation of the Cascadia subduction zone. *Journal of Geophysical Research: Solid Earth*, 108(B1), 2003.
108. Pei-Ling Wang, Simon E Engelhart, Kelin Wang, Andrea D Hawkes, Benjamin P Horton, Alan R

Nelson, and Robert C Witter. Heterogeneous rupture in the great Cascadia earthquake of 1700 inferred from coastal subsidence estimates. *Journal of Geophysical Research: Solid Earth*, 118(5):2460–2473, 2013.
109. Susanna I. Webb. *Interaction of structure and physical properties in accretionary wedges: examples from the Cascadia and Nankai Trough subduction zones*. PhD thesis, University of Wisconsin - Madison, 2017.
110. Johannes Weertman. Unstable slippage across a fault that separates elastic media of different elastic constants. *Journal of Geophysical Research: Solid Earth*, 85(B3):1455–1461, 1980.
111. James Wendt, David D Oglesby, and Eric L Geist. Tsunamis and splay fault dynamics. *Geophysical Research Letters*, 36(15), 2009.
112. Robert C Witter, Harvey M Kelsey, and Eileen Hemphill-Haley. Great Cascadia earthquakes and tsunamis of the past 6700 years, Coquille River estuary, southern coastal Oregon. *Geological Society of America Bulletin*, 115(10):1289–1306, 2003.

11 Supplementary Figures

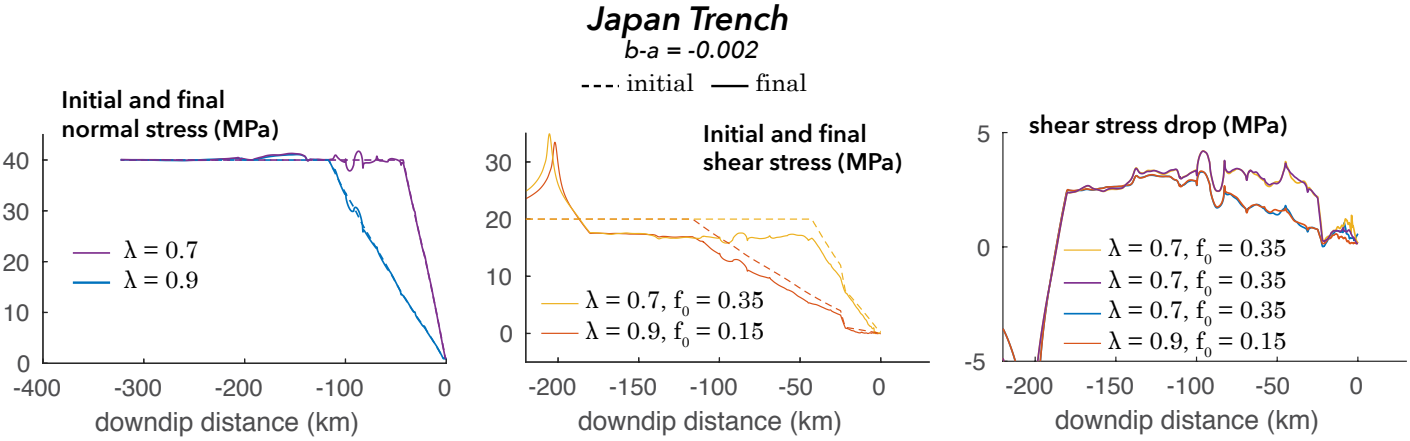

Fig. 21 Initial and final normal stress, initial and final shear stress, and shear stress drop for simulations of the Japan Trench. All simulations shown with $b - a = -0.002$. Stress drops are larger for $\lambda = 0.7$.

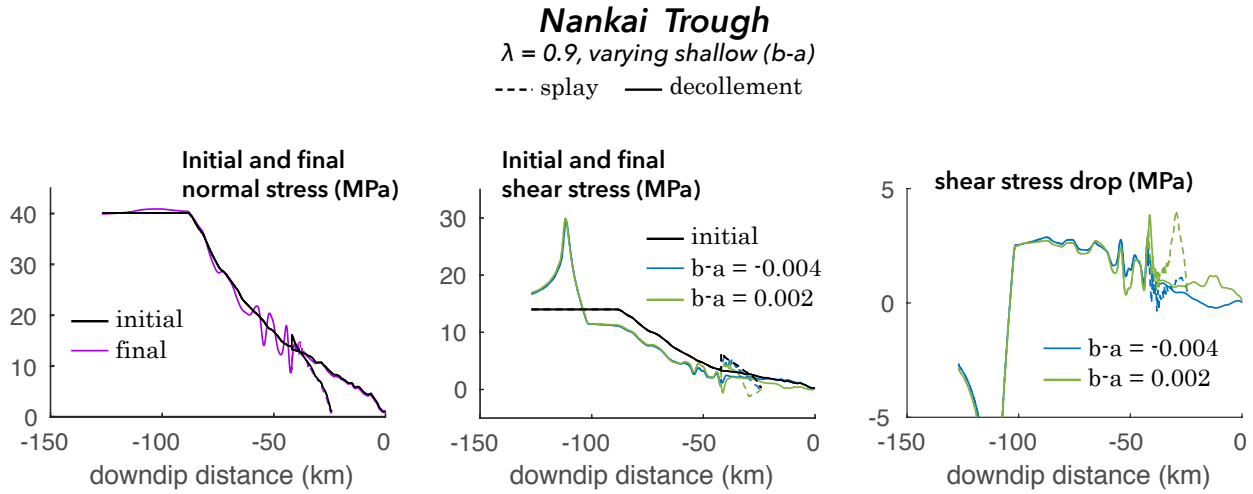

Fig. 22 Initial and final normal stress, initial and final shear stress, and shear stress drop for simulations of the Nankai Trough. All simulations shown with $\lambda = 0.9$. Shallow stress drops are greater for larger $b - a$.

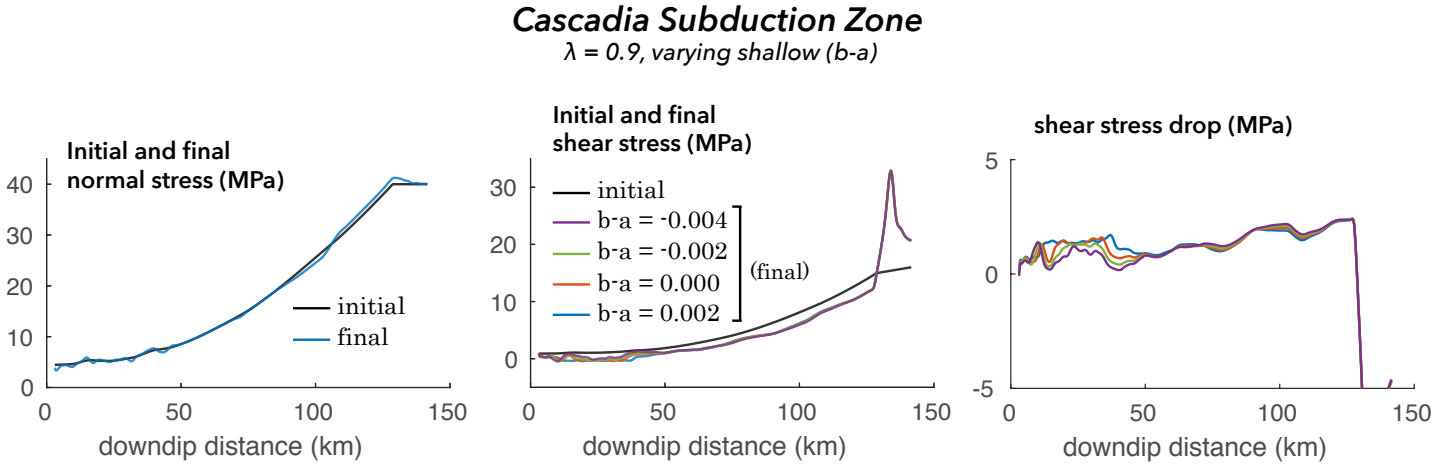

Fig. 23 Initial and final normal stress, initial and final shear stress, and shear stress drop for simulations of the Cascadia Subduction Zone. All simulations shown with $\lambda = 0.9$. Shallow stress drops are greater for larger $b - a$.

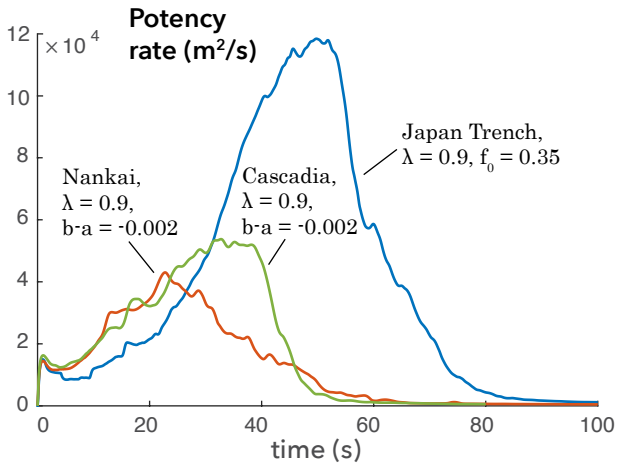

Fig. 24 A comparison of potency rate for the three subduction zones, all with $b - a = -0.002$ and $\lambda = 0.9$.